

Multiplicative-Regularized FFT Twofold Subspace-Based Optimization Method for Inverse Scattering Problems

Kuiwen Xu, Yu Zhong, Rencheng Song, Xudong Chen, *Member, IEEE*, and Lixin Ran

Abstract—In this paper, we combine two techniques together, i.e., the fast Fourier transform-twofold subspace-based optimization method (FFT-TSOM) and multiplicative regularization (MR) to solve inverse scattering problems. When applying MR to the objective function in the FFT-TSOM, the new method is referred to as MR-FFT-TSOM. In MR-FFT-TSOM, a new stable and effective strategy of regularization has been proposed. MR-FFT-TSOM inherits not only the advantages of the FFT-TSOM, i.e., lower computational complexity than the TSOM, better stability of the inversion procedure, and better robustness against noise compared with the SOM, but also the edge-preserving ability from the MR. In addition, a more relaxed condition of choosing the number of current bases being used in the optimization can be obtained compared with the FFT-TSOM. Particularly, MR-FFT-TSOM has even better robustness against noise compared with the FFT-TSOM and multiplicative regularized contrast source inversion (MR-CSI). Numerical simulations including both inversion of synthetic data and experimental data from the Fresnel data set validate the efficacy of the proposed algorithm.

Index Terms—Fast Fourier transform-twofold subspace-based optimization method (FFT-TSOM), inverse scattering, multiplicative regularization (MR), optimization, subspace.

27

I. INTRODUCTION

INVERSE scattering problems have been of interest for many years, the same being widely applied in medical imaging, geophysics, biological studies, nondestructive testing and evaluation, through-wall imaging, etc. The goal of the inversion mainly considers the reconstruction of the location, the shape, the quantity, and the electric constitutive parameters of unknown objects inside a bounded domain of interest (DoI) immersed in a known background medium including, i.e., permittivity and conductivity, when the object is illuminated by a series of known incident electromagnetic waves.

Manuscript received June 19, 2013; revised December 11, 2013, March 25, 2014, and May 24, 2014; accepted May 29, 2014. This work was supported in part by the Singapore Temasek Defence Systems Institute under Grant TDSI/11-010/1A and in part by Institute Fresnel and the National Natural Science Foundation of China under Grant 61131002 and Grant 61071063.

K. Xu and L. Ran are with the Laboratory of Applied Research on Electromagnetics (ARE), Zhejiang University, Hangzhou 310027, China (e-mail: kuiwenxu@gmail.com; ranlx@zju.edu.cn).

Y. Zhong is with the A*STAR, Institution of High Performance Computing, Singapore 138632 (e-mail: zhongyu@ihpc.a-star.edu.sg).

R. Song and X. Chen are with the Department of Electrical and Computer Engineering, National University of Singapore, Singapore 117576 (e-mail: elezhong@nus.edu.sg; dr.csong@gmail.com; elechenx@nus.edu.sg).

Color versions of one or more of the figures in this paper are available online at <http://ieeexplore.ieee.org>.

Digital Object Identifier 10.1109/TGRS.2014.2329032

To deal with intrinsical nonlinearity and ill-posedness, many iterative algorithms have been proposed so far, such as the Born iterative method [1], the distorted Born iterative method [2]–[4], the contrast source inversion (CSI) method [5], [6], Gauss–Newton-type methods [7]–[9], the multilevel linear sampling method [10], and other stochastic type of inversion methods such as the genetic algorithm and the evolutionary algorithm [11]–[13]. Moreover, recently, to reduce the degree of nonlinearity of the relationship among the data and the unknowns, as well as the overall computational burden, the contrast-source-extended Born inversion methods are quickly exploited [14]–[18]. Indeed, these works have shed some light on the territory of how the most difficult inverse scattering problems can be solved. In most of the aforementioned algorithms, regularization techniques are applied so as to stabilize the solvers. These regularization techniques are mainly proposed from a mathematical point of view, such as the Tikhonov regularization, minimization of total variation, and so on. Particularly, van den Berg *et al.* investigated a multiplicative form total variation regularization together with the CSI, i.e., the multiplicative regularized contrast source inversion (MR-CSI) technique [6], [19]–[23]. Using the L_1 - and L_2 -norm total variation, where the weighting parameter is prescribed by the error norm of the original objective function in CSI so as to avoid the uncertainty and unpredictability of the weighting parameters [6], [21], the MR-CSI obtains quite satisfactory results with preserving edges of shapes of unknown scatters.

Recently, a subspace-based optimization method (SOM) has been proposed for reconstructing the dielectric profile of scatterers from scattered fields in both 2-D and 3-D electromagnetic inverse scattering problems [24]–[28]. The SOM utilizes the spectral property of the mapping from the induced current to measured scattered fields and determines part of the induced current in the DoI and obtains the remaining part of the induced current by the optimization. By doing so, the SOM only searches the solution within a subspace of the whole current space and, thus, stabilizes the solution to some extent. Given the SOM, a twofold SOM (TSOM) is further proposed to utilize the spectral property of the mapping from the induced current to the scattered fields in the DoI [29], [30], in which the remaining parts of the induced current are constructed using a new set of orthogonal basis according to their influence on the fields inside the DoI. By choosing a small number of bases, the optimization problem therein is simplified owing to the current subspace used with only the most influential bases and, thus,

83 with much smaller dimensions than the one used in the SOM.
 84 Given a good approximation to the original physical modeling
 85 and much smaller number of unknowns, the TSOM achieves
 86 better stability and better robustness against noise compared
 87 with the SOM.

88 In the TSOM, to obtain the spectral information of the map-
 89 ping from the current to the fields inside the domain, singular
 90 value decomposition (SVD) of the mapping is needed, which
 91 might cost a lot of computational resources when the problem
 92 is not a small-scale one. To further accelerate the optimization
 93 and avoid the computationally burdensome SVD, a fast Fourier
 94 transform (FFT) TSOM has been proposed by using the current
 95 subspace constructed by discrete Fourier bases that is a good
 96 approximation to the original current subspace spanned by sin-
 97 gular vectors [31]. In the aforementioned literatures, the FFTs
 98 are usually solely used as an acceleration of the multiplication
 99 of Green's function and the induced current. Moreover, the
 100 Fourier bases are used to represent the dielectric profile as
 101 well [32]–[34]. However, though it might reduce the number
 102 of unknowns a bit, such a representation of the profile does not
 103 help much on addressing the ill-posedness and nonlinearity of
 104 the problem. Our use of the Fourier bases in FFT-TSOM is on
 105 constructing the induced current. Moreover, the FFT-TSOM not
 106 only inherits the merits of TSOM including better stability and
 107 better robustness against noise compared with the SOM but also
 108 dramatically reduces the computational complexity compared
 109 with the TSOM. To obtain the best stability of the solver, both
 110 the FFT-TSOM and the TSOM need to gradually increase the
 111 number of bases in different phase of the optimization. Such
 112 a lower-dimension technique for the current subspace can be
 113 considered as a physical regularization, which is different from
 114 those aforementioned mathematical regularizations.

115 Due to the fact that they are different types of regulariza-
 116 tion techniques, in this paper, we combine the two techniques
 117 together, i.e., the FFT-TSOM and multiplicative regularization
 118 (MR). The purpose of doing so is to propose a new com-
 119 pound regularization technique that outperforms the original
 120 two methods with better robustness against noise. Due to the
 121 difference between the FFT-TSOM and the CSI, when applying
 122 the MR to the objective function in FFT-TSOM, one needs to
 123 adjust the MR parameter accordingly, which will be discussed
 124 in detail in this paper. After applying the MR technique to
 125 the FFT-TSOM, the new method, which is referred to as MR-
 126 FFT-TSOM, is tested with different dielectric profiles, and the
 127 numerical results show that the MR-FFT-TSOM presents some
 128 new properties: 1) As expected, the MR-FFT-TSOM preserves
 129 the advantages of the original FFT-TSOM, i.e., better stability
 130 and robustness against noise compared with the original SOM
 131 and MR-CSI, and also inherits the edge-preserving ability from
 132 the MR; 2) after introducing the MR, the MR-FFT-TSOM has a
 133 more relaxed condition of choosing the number of current bases
 134 being used in the optimization compared with the FFT-TSOM,
 135 which makes MR-FFT-TSOM easier to implement; 3) the new
 136 MR-FFT-TSOM has even better robustness against noise com-
 137 pared with the FFT-TSOM and MR-CSI; 4) a new strategy of
 138 the regularization parameter has been proposed and makes MR-
 139 FFT-TSOM more robust and stable. The give properties have
 140 been tested by noisy synthetic data and the Fresnel data set.

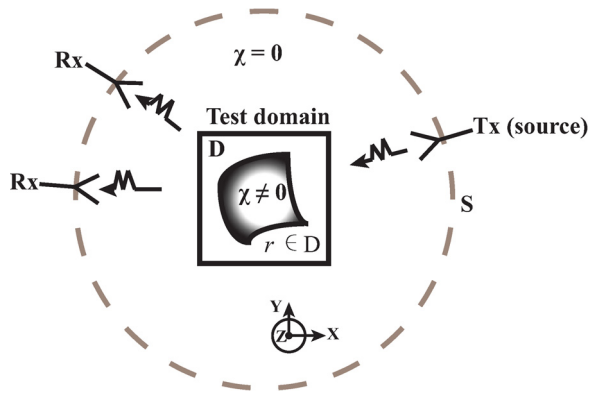


Fig. 1. Basic geometrical model of the inverse scattering problem.

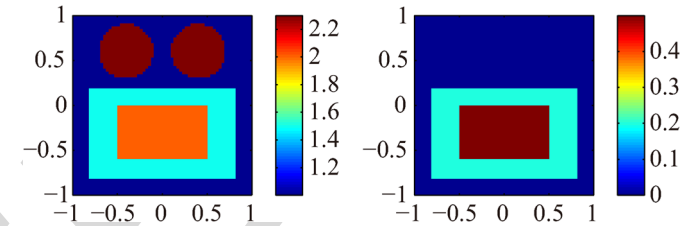


Fig. 2. Exact profile mentioned in [31], the (left) real and (right) imaginary part of the relative permittivity ϵ_r .

II. FORMULATION OF THE PROBLEM

Here, a 2-D electromagnetic inverse scattering problem with 142 the transverse magnetic (TM) incidence is considered. The 143 model of the 2-D inverse scattering problems consists of a 144 bounded DoI $D(D \subset \mathbb{R}^2)$, where nonmagnetic scatterers are 145 located with unknown permittivity $\epsilon(\bar{r}), \bar{r} \in D$, and the back- 146 ground homogeneous medium with permittivity ϵ_b , permeabil- 147 ity μ_b , and wavenumber $k_b = \omega/\sqrt{\epsilon_b \mu_b}$, $\mu_b = \mu_0$. Let us say 148 there are a total of N_i incidences from line sources at a single 149 frequency located at $\bar{r}_l^i, l = 1, 2, \dots, N_i$ in the domain (or on 150 curve) S outside of D , and these incident fields are denoted 151 as \bar{E}_l^{inc} . For each incidence, the scattered electric fields are 152 measured by N_r antennas located at $r_q^s, q = 1, 2, \dots, N_r$, as 153 depicted in Fig. 1. The complex contrast in the DoI is defined 154 as $\chi(\bar{r}) = (\epsilon(\bar{r}) - \epsilon_b)/\epsilon_b$. In the inverse problem, we need to 155 determine $\epsilon(\bar{r})$, given a set of $N_i N_r$ scattering data, \bar{E}_l^{sca} . The 156 test domain D in the $x - y$ plane is discretized into many small 157 rectangular subdomains with a smaller than $1/10$ wavelength 158 dimension and centered at \bar{r}_m . The total number of subdomains 159 is M . In this paper, the domains of interest are chosen to be 160 rectangular to implement the conjugate gradient fast Fourier 161 transform (CG-FFT) scheme and apply the FFT algorithm with 162 the new Fourier bases (see Fig. 2).

What follows is a quick review of the FFT-TSOM, and more 164 details can be found in [31]. The method of moments (MoM) is 165 used to discretize the original Lippmann–Schwinger equation. 166 For the l th incidence, the total electric field at the center of the 167 m th subunit $\bar{E}_{l;m}^{\text{tot}}$ is given by

$$\bar{E}_{l;m}^{\text{tot}} = \bar{E}_{l;m}^{\text{inc}} + \sum_{n=1}^M \bar{G}_D(\bar{r}_m, \bar{r}_n) \cdot \bar{I}_{l;n}, \quad m = 1, 2, \dots, M \quad (1)$$

169 where $\bar{E}_{l;n}^{\text{inc}}$ is the incident electric field at \bar{r}_m , and $\bar{I}_{l;n}$ is the
 170 induced current at \bar{r}_n , which can be related to the total electric
 171 filed $\bar{E}_{l;n}^{\text{tot}}$ by

$$\bar{I}_{l;n} = -i\omega\varepsilon_b\chi_n \bar{E}_{l;n}^{\text{tot}}, \quad n = 1, 2, \dots, M. \quad (2)$$

172 $\bar{G}_D(\bar{r}_m, \bar{r}_n)$ denotes the Green function of the background
 173 media.

174 It is convenient to write (1) and (2) in compact form as

$$\bar{I}_l = -i\omega\varepsilon_b\bar{\chi} \cdot (\bar{E}_l^{\text{inc}} + \bar{G}_D \cdot \bar{I}_l) \quad (3)$$

175 where $\bar{I}_l = [I_{l;1}(r_1), I_{l;2}(r_2), \dots, I_{l;M}(r_M)]^T$ is an M -
 176 dimensional vector, i.e., $\bar{E}_l^{\text{inc}} = [E_{l;1}^{\text{inc}}, E_{l;2}^{\text{inc}}, \dots, E_{l;M}^{\text{inc}}]^T$, and
 177 superscript T denotes the transpose operator.

178 The integral operator relating the induced current and the
 179 scattered fields can be expressed as

$$\bar{E}_l^{\text{sca}} = \bar{G}_S \cdot \bar{I}_l, \quad l = 1, 2, \dots, N_i \quad (4)$$

180 where $\bar{E}_l^{\text{sca}} = [E_l^{\text{sca}}(r_1^s), E_l^{\text{sca}}(r_2^s), \dots, E_l^{\text{sca}}(r_{N_r}^s)]^T$, \bar{G}_S is an
 181 $N_r \times M$ matrix with elements $\bar{G}_S(\bar{r}_q^s, \bar{r}_m)$ being Green's func-
 182 tion from the DoI to the measurement. Equations (3) and (4)
 183 are considered as the current equation and the field equation,
 184 respectively (or the state equation and the data equation referred
 185 to in [26]).

186 From [26], with the spectral information from the SVD of
 187 $\bar{G}_S(\bar{G}_S \cdot \bar{v}_j^S = \sigma_j^S \bar{u}_j^S)$, the induced current is split into two parts
 188 in the SOM, i.e., the deterministic portion and the ambiguous
 189 part, the former of which can be obtained by

$$\bar{I}_l^d = \sum_{j=1}^L \bar{u}_j \frac{\bar{v}_j^S}{\sigma_j^S} \bar{v}_j^S = \bar{V}_S^+ \cdot \bar{\alpha}_l^+ \quad (5)$$

190 where $\bar{V}_S^+ = [\bar{v}_1^S, \bar{v}_2^S, \dots, \bar{v}_L^S]$, and $\bar{\alpha}_l^+ = [\alpha_{l;1}^+, \alpha_{l;2}^+, \dots,$
 191 $\alpha_{l;L}^+]^T$, $\alpha_{l;j}^+ = (\bar{u}_j^S \cdot \bar{E}_l^{\text{sca}})/\sigma_j^S, j = 1, 2, \dots, L$, superscript *
 192 denotes the Hermitian operation, whereas superscript + refers
 193 to the dominant current space, the subspace corresponding
 194 to the dominant singular values. The value of L is chosen
 195 according to the singular values of \bar{G}_S and the level of noise
 196 [24], [26]. On the other hand, as mentioned in the TSOM [29],
 197 we can express the ambiguous part of the induced current as

$$\bar{I}_l^a(\bar{\beta}_l) = \bar{V}_D^+ \cdot \bar{\beta}_l \quad (6)$$

198 where $\bar{\beta}_l$ is an M_0 -dimensional vector, and the corresponding
 199 current subspace \bar{V}_D^+ can be expressed as

$$\bar{V}_D^+ = \left(\bar{I}_M - \bar{V}_S^+ \cdot \bar{V}_S^{+*} \right) \cdot \bar{V}_D^+ \quad (7)$$

200 where $\bar{V}_D^+ = [\bar{v}_1^D, \bar{v}_2^D, \dots, \bar{v}_{M_0}^D]$ is the current subspace
 201 spanned by the singular vectors to the largest M_0 singular
 202 values of the operator \bar{G}_D [29], [30]. However, to avoid the
 203 computational burdensome SVD of the operator \bar{G}_D and further
 204 accelerate the process of optimization, the original current sub-
 205 space spanned by the singular vector bases can be substituted

206 by the discrete Fourier bases such that the FFT-TSOM was
 207 proposed in [31]. Thus

$$\begin{aligned} \bar{I}_l^a &= \left(\bar{I}_M - \bar{V}_S^+ \cdot \bar{V}_S^{+*} \right) \cdot [\bar{F}_1^D, \bar{F}_2^D, \dots, \bar{F}_{M_0}^D] \cdot \bar{\beta}_l \\ &= \left(\bar{I}_M - \bar{V}_S^+ \cdot \bar{V}_S^{+*} \right) \cdot \text{vec}\{\text{IDFT}\{\bar{\gamma}_l\}\} \end{aligned} \quad (8)$$

208 where $\bar{F}_j, j = 1, 2, \dots, M_0$ are the vectorized discrete Fourier
 209 bases, and $\bar{\gamma}_l$ is the 2-D Fourier coefficient tensor with nonzero
 210 elements corresponding to those low-frequency discrete Fourier
 211 bases (denoted as four blocks with size M_F in the four cor-
 212ners of the coefficient tensor in MATLAB) and zero elements
 213 corresponding to the remaining high-frequency discrete Fourier
 214 bases. The $\text{vec}\{\cdot\}$ is the vectorization operator. As mentioned
 215 in [31], low-frequency Fourier bases can be used to construct a
 216 current subspace as the approximation to the original current
 217 subspace spanned by the singular vectors with large singu-
 218 lar values. The inverse discrete Fourier transform (IDFT) is
 219 performed by the 2-D FFT algorithm, and the computational
 220 complexity is $O(M \log_2 M)$, which is much smaller than the
 221 one of the direct multiplication in the TSOM. Detail of the FFT-
 222 TSOM could be found in [31].

223 After constructing the induced current in the aforementioned
 224 way, the objective function is defined as below. First, the
 225 mismatch of the scattered fields is defined as

$$\Delta_l^{\text{fe}}(\bar{\beta}_l) = \|\bar{G}_S \cdot \bar{I}_l^a + \bar{G}_S \cdot \bar{I}_l^d - \bar{E}_l^{\text{sca}}\|^2 \quad (9)$$

226 where $\|\cdot\|$ is the Euclidean length of a vector. Similarly, the
 227 current equation is another key equation to satisfy. The residue
 228 in the current equation is defined to be [31]

$$\Delta_l^{\text{cur}}(\bar{\beta}_l, \bar{\chi}) = \|\bar{\mathcal{L}}_{\text{SOM}}(\bar{\beta}_l) - \bar{\Gamma}_l\|^2 \quad (10)$$

229 where $\bar{\mathcal{L}}_{\text{SOM}}(\bar{\beta}_l) = (\bar{I}_l^a(\bar{\beta}_l)/-i\omega\varepsilon_b) - \bar{\chi} \bar{G}_D \cdot \bar{I}_l^a(\bar{\beta}_l)$, and $\bar{\Gamma}_l = 229$
 230 $\bar{\chi}(\bar{E}_l^{\text{inc}} + \bar{G}_D \cdot \bar{I}_l^d) + \bar{I}_l^d/i\omega\varepsilon_b$. Finally, the objective function 230
 231 of FFT-TSOM is

$$f_T(\bar{\beta}_l, \bar{\chi}) = \sum_{l=1}^{N_i} (F_D(\bar{\beta}_l) + F_S(\bar{\beta}_l, \bar{\chi})) \quad (11)$$

232 where $F_D(\bar{\beta}_l) = \Delta_l^{\text{fe}}(\bar{\beta}_l)/\|\bar{E}_l^{\text{sca}}\|^2$, and $F_S(\bar{\beta}_l, \bar{\chi}) = 232$
 233 $\Delta_l^{\text{cur}}(\bar{\beta}_l, \bar{\chi})/\|\bar{E}_l^{\text{inc}}\|^2$. The optimization is to minimize 233
 234 the objective function (11).

III. REGULARIZATION AND INVERSION ALGORITHM

235 Recently, to stabilize the solution of the inverse scattering
 236 problem, van den Berg and Kleinmann (1995) incorporated
 237 the total variation (TV) in an inverse scattering problem by
 238 enhancing the modified gradient algorithm [35]. After that, the
 239 multiplicative regularization technique is introduced in the MR-
 240 CSI method based on the L_1 - and L_2 -norm TV as constraint
 241 [20], [21]. In the MR-CSI method, the objective function is
 242 composed of the original cost function, and the multiplicative
 243 regularizer with a weighted L_2 -norm TV. The weighting param-
 244 eter is determined and updated by the inversion result during the
 245 optimization process.

247 However, the strategy of the regularization parameter used in
 248 the MR-CSI cannot be directly used in the FFT-TSOM. In the
 249 FFT-TSOM, only the most influential bases are utilized. Hence,
 250 the residues in the current equation and the filed equation in the
 251 FFT-TSOM could be much larger than the one in the CSI. In
 252 this paper, a novel adaptive regularization parameter updating
 253 strategy will be introduced.

254 First, with the inclusion of the multiplicative regularizer,
 255 the objective function, at the n th iteration of the optimization,
 256 becomes

$$\mathcal{H}_n(\bar{\beta}_l, \bar{\chi}) = f_T(\bar{\beta}_l, \bar{\chi}) \cdot F_n^{\text{MR}}(\chi) \quad (12)$$

257 where $\bar{\beta}_l$ and $\bar{\chi}$ are the unknowns, and the multiplicative
 258 regularizer is given as in [21]

$$F_n^{\text{MR}}(\chi) = \frac{1}{A} \int_D \frac{|\nabla \chi(\bar{r})|^2 + \delta_n^2}{|\nabla \chi_{n-1}(\bar{r})|^2 + \delta_n^2} d\bar{v}(\bar{r}) \quad (13)$$

259 where A is the area of the test domain D , and ∇ denotes the
 260 spatial differentiation with respect to \bar{r} . The constant regular-
 261 ization parameter δ_n^2 is introduced for restoring differentiability
 262 of the TV regularizer, and it plays a crucial role in the TV-
 263 type regularization. From [20], the effect of the regularization
 264 should be increased as a function of the number of the iterations
 265 by decreasing the regularization parameter δ_n^2 . Therefore, in
 266 the MR-CSI method, the regularization parameter is chosen as
 267 follows:

$$\delta_{\text{CSI}}^2 = \frac{F_S(\bar{\beta}_l, \bar{\chi})}{\Delta^2} \quad (14)$$

268 where Δ is the mesh size of the discretized domain D . Equation
 269 (14) is designed such that the value of δ_n^2 is decreased with
 270 the value of the objective function; thus, as the iterations
 271 proceed, the effect of multiplicative regularization is increased.
 272 In the beginning of optimization procedure, δ_n^2 is equal to δ_{CSI}^2 ,
 273 and when δ_{CSI}^2 almost keeps unchanged, then δ_n^2 is gradually
 274 reduced to a threshold by an exponential function, which can
 275 make sure that the problem remains convex [21]. The specific
 276 expression of δ_n^2 is given in the following algorithm sketch.

277 Following the names of two predecessors, the new inversion
 278 method is named as MR-FFT-TSOM, and it is implemented as
 279 follows:

280 Step 1) Calculate \bar{G}_S , \bar{G}_D , and the thin SVD of \bar{G}_S ; obtain
 281 \bar{I}_l^d from (6), $l = 1, 2, \dots, N_i$.

282 Step 2) Initialization, $n = 0$; $\bar{\chi}_0 = 0$; select M_F , and initial-
 283 ize $\bar{\beta}_{l,0} = 0$ according to the method in FFT-TSOM
 284 [31], $\bar{\rho}_{\beta;l,0}$ and $\bar{\rho}_{\varepsilon;0}$ are the search direction of $\bar{\beta}_l$ and
 285 $\bar{\chi}$, respectively. $\bar{\rho}_{\beta;l,0} = 0$ and $\bar{\rho}_{\varepsilon;0} = 0$.

286 Step 3) $n = n + 1$

287 Step 3.1) Update $\bar{\beta}_{l,n}$: $\bar{\beta}_{l,n} = \bar{\beta}_{l,n-1} + d_{\beta;l,n} \bar{\rho}_{\beta;l,n}$,
 288 where the scalar $d_{\beta;l,n}$ can be obtained
 289 according to $(\partial f_T / \partial d_{\beta;l,n}) = 0$. Calcu-
 290 late gradient (Frechet derivative) $\bar{g}_{\beta;l,n} =$
 291 $\nabla_{\bar{\beta}_l} f_T$ evaluated at $\bar{\beta}_{l,n-1}$ and $\bar{\chi}_{n-1}$; de-
 292 termine the CG search directions $\bar{\rho}_{\beta;l,n} =$
 293 $\bar{g}_{\beta;l,n} + (\text{Re}(\bar{g}_{\beta;l,n} - \bar{g}_{\beta;l,n-1}, \bar{g}_{\beta;l,n}) / \| \bar{g}_{\beta;l,n} \|)^2 \bar{\rho}_{\beta;l,n-1}$, $n \geq 1$ [6], [26].

295 Step 3.2) There are two step operations for updating 295
 296 the contrast, including before regulariza- 296
 297 tion and after regularization, respectively. 297
 298 Update the contrast before multiplicative 298
 299 regularization $\bar{\chi}_n^{\text{BMR}}$: for the m th subunit, 299
 300 $m = 1, 2, \dots, M$, utilizing $(\partial f_T / \partial \chi) = 0$, 300
 301 the solution is given by

$$\left(\bar{\chi}_n^{\text{BMR}} \right)_m = \frac{\sum_{l=1}^{N_i} \left(\bar{E}_{l,n}^{\text{tot}} \right)_m^* \cdot \left(\frac{\bar{I}_{l,n}}{-i\omega\varepsilon_b} \right)_m / \left\| \bar{E}_l^{\text{inc}} \right\|^2}{\sum_{l=1}^{N_i} \left(\bar{E}_{l,n}^{\text{tot}} \right)_m^* \cdot \left(\bar{E}_{l,n}^{\text{tot}} \right)_m / \left\| \bar{E}_l^{\text{inc}} \right\|^2} \quad (15)$$

302 where $(\bar{I}_{l,n})_m = (\bar{I}_{l,n}^d)_m + (\bar{I}_{l,n}^a)_m$ and 302
 303 the corresponding total electrical field in 303
 304 the m th subunit $(\bar{E}_{l,n}^{\text{tot}})_m = (\bar{E}_{l,n}^{\text{inc}})_m + 304$
 305 $(\bar{G}_D \cdot \bar{I}_{l,n})_m$. 305

306 Step 3.3) Update δ_n^2 : According to the obtained 306
 307 $\bar{\chi}_n^{\text{BMR}}$ and $\bar{\beta}_{l,n}$, calculate the $F_D(\bar{\beta}_{l,n})$ 307
 308 and $F_S(\bar{\beta}_{l,n}, \bar{\chi}_n^{\text{BMR}})$. When $n > 5$, if six 308
 309 consecutive values of $\delta_{\text{CSI}}^2 = F_S(\bar{\beta}_{l,n}, 309$
 $\bar{\chi}_n^{\text{BMR}}) / \Delta^2$ nearly keep unchanged, then 310
 $\delta_n^2 = \delta_{\text{CSI}}^2 \times e^{-(\alpha(M_u/2-M_F)(n-N_\kappa)/N_\kappa)}$, 311
 312 where M_F is the size of blocks in the 312
 313 four corners of the coefficient tensor [31], 313
 314 and N_κ is the iteration number when the 314
 315 average of the previous five consecutive 315
 316 variance of δ_{CSI}^2 is less than a small con- 316
 317 stant value κ ($\kappa = \delta_{\text{CSI}}^2 / 10$), M_u is simply 317
 318 chosen as the smaller number of of M_x 318
 319 and M_y , which are the total number of 319
 320 cells along the x - and y -directions, repe- 320
 321 tively, and we assume that $M_x \leq M_y$ here, 321
 322 regardless if the domain is rectangular 322
 323 or square, and the value of $\alpha > 0$ will be 323
 324 discussed in the numerical simulation 324
 325 part. The reason we choose such a 325
 326 parameter is that, as the optimization 326
 327 proceeds, the regularization effect will 327
 328 become strong even when using the FFT- 328
 329 TSOM model ing. Otherwise, $\delta_n^2 = \delta_{\text{CSI}}^2$. 329
 330 On the other hand, as mentioned 330
 331 in [21], to keep convexity for real 331
 $d_{\varepsilon,n}$, δ_n^2 should be larger than the value 332
 $(1/2)(\|\nabla \chi_n / \sqrt{A(|\nabla \chi_n|^2 + \delta_{n-1}^2)}\|_D^2 / \|1 / 333$
 $\sqrt{A(|\nabla \chi_n|^2 + \delta_{n-1}^2)}\|_D^2)$. 334

335 Step 3.4) Update $\bar{\chi}_n^{\text{MR}}$ (the contrast after multi- 335
 336 plicative regularization): The regularized 336
 337 updated contrast $(\bar{\chi}_n^{\text{MR}})_m = (\bar{\chi}_n^{\text{BMR}})_m + 337$
 $(d_{\varepsilon,n} \bar{\rho}_{\varepsilon,n})_m$ where $\bar{\rho}_{\varepsilon,n}$ is the conjugate 338
 339 gradient direction $\bar{\rho}_{\varepsilon,n} = \bar{g}_{\varepsilon,n} + (\text{Re} \times 339$
 $\langle \bar{g}_{\varepsilon,n} - \bar{g}_{\varepsilon,n-1}, \bar{g}_{\varepsilon,n} \rangle / \bar{g}_{\varepsilon,n} \bar{\rho}_{\varepsilon,n-1}, n \geq 1)$, 340
 $\bar{g}_{\varepsilon,n} = (\nabla_{\chi} \mathcal{H}_n(\bar{\beta}_l, \bar{\chi}) / \sum_{l=1}^{N_i} \|\bar{E}_{l,n}^{\text{tot}}\|^2)$ eval- 341
 342 uated at $\bar{\chi}_n^{\text{BMR}}$ with the previous mini- 342
 343 mization before regularization when the 343

gradient of $F_S(\bar{\beta}_{l,n}, \bar{\chi})$ with respect to the changes in the contrast around the point $\bar{\chi} = \bar{\chi}_n^{\text{BMR}}$ vanishes. Thus, $\bar{g}_{\varepsilon,n} = (F_D \times (\bar{\beta}_{l,n}) + F_S(\bar{\beta}_{l,n}, \bar{\chi}))((\partial F_n^{\text{MR}}(\chi)/\partial \chi)_\chi = \chi_n^{\text{BMR}} / \sum_{l=1}^{N_i} \|\bar{E}_{l,n}^{\text{tot}}\|^2)$ being a preconditioned gradient of the regularization factor $F_n^{\text{MR}}(\chi)$ with respect to the changes in the contrast around the point $\chi = \chi_n^{\text{BMR}}$. In addition, the real parameter $d_{\varepsilon,n}$ can be found from a line minimization as done in [20].

Step 4) if the termination condition is satisfied, stop optimization. Otherwise, go to step 3. Empirically, we stop the optimization when the values of the contrast do not noticeably change for successive five iterations.

We mention in passing that when the MR is applied to SOM, the optimization procedure can be considered as a special case of the aforementioned procedure where all the Fourier bases in MR-FFT-TSOM are used, i.e., the MR-SOM can be considered as a special case of MR-FFT-TSOM.

IV. NUMERICAL EXPERIMENT AND DISCUSSION

Here, to test the proposed MR-FFT-TSOM, we present several numerical examples in the 2-D TM case. In all tests in this section, additive white Gaussian noise (AWGN) is added to the numerical scattering results and is quantified by $(\|\bar{e}_l\|/\|\bar{e}_l\|/\|\bar{E}_{l,\text{MOM}}^{\text{sca}}\|/\|\bar{E}_{l,\text{MOM}}^{\text{sca}}\|) \times 100\%$, where $\bar{E}_{l,\text{MOM}}^{\text{sca}}$ is the numerical scattering results for the l th incidence, so that $\bar{E}_l^{\text{sca}} = \bar{E}_{l,\text{MOM}}^{\text{sca}} + \bar{e}_l$. The $\bar{E}_{l,\text{MOM}}^{\text{sca}}$ are generated by MoM using finer grid meshes than the ones used in the inversions.

In the following tests, the DoI is a $2 \text{ m} \times 2 \text{ m}$ square centered at the origin. The scatterers are illuminated by 16 incidences at 400 MHz (the corresponding wavelength $\lambda = 0.75 \text{ m}$) incident from different angles evenly distributed in $[0, 2\pi]$ on a circle with 3-m radius centered at the origin. The scattered fields are collected by an antenna array with 32 antennas uniformly distributed along the same circle with 3-m radius. In all the simulations, a 64×64 grid mesh of the DoI is used for our reconstructions. As for the scattered fields in the forward-scattering problem, they are calculated by the MoM method with a 100×100 grid mesh. We choose the $L = 15$ throughout through all the simulations as in [26].

In the first case, we considered the profile mentioned in [31], which consists of two discs, a coated rectangle, and the background material, as shown in Fig. 1. The two disks are centered at $(-0.4, 0.6) \text{ m}$ and $(0.4, 0.6) \text{ m}$ with the same 0.3-m radius and the same relative permittivity $\varepsilon_r = 2.3$, $\varepsilon_r = \varepsilon/\varepsilon_b$. The coated rectangle is centered at $(0, -0.3) \text{ m}$. The inner rectangle has a 1-m-long edge and a 0.6-m-short range, whereas the outer rectangle has a 1.6-m-long edge and a 1-m-short edge. The relative permittivity of the inner rectangle is $\varepsilon_r = 2 + i0.5$, whereas the outer one is $\varepsilon_r = 1.5 + i0.2$.

As we know in [31], the SOM cannot obtain a basic and satisfactory reconstruction result of the given profile. As depicted in Fig. 3, when the noise level is 10% AWGN, if we

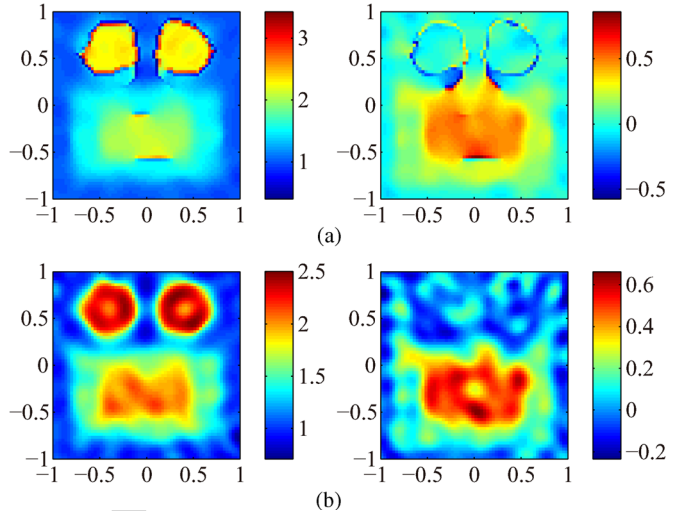


Fig. 3. Reconstruction results by MR-SOM with 10% AWGN, the (left) real and (right) imaginary part of the reconstruction relative permittivity ε_r when (a) $\delta_n^2 = \delta_{\text{CSI}}^2$ and (b) $\delta_n^2 = \delta_{\text{CSI}}^2 \times 2^3$ after 1000 iterations.

use the $\delta_{\text{CSI}}^2 = F_S(\bar{\beta}_l, \bar{\chi})/\Delta^2$ directly from the paper of van den Berg [21], the results in Fig. 3(a) show that MR works in the MR-SOM but cannot attain the expected effect compared with the exact profile. However, if the regularization parameter is modified to $\delta_n^2 = \delta_{\text{CSI}}^2 \times 2^3$, a significant change can be observed in Fig. 3(b), where the permittivity of the profile is more accurate, and a better effect on edge preserving can be observed compared with Fig. 3(a). Under the 30% AWGN, the reconstruction results are shown in Fig. 4, the result after 1000 iterations in Fig. 4(a) utilizing the regularization parameter δ_{CSI}^2 is significantly better than $\delta_n^2 = \delta_{\text{CSI}}^2 \times 2^3$ after 1500 iterations in Fig. 4(b), in which the reconstruction result almost cannot be recognized. This is probably due to the reason that, when the noise level is higher, the residue of the current equation is larger, i.e., $F_S(\bar{\beta}_l, \bar{\chi})$, and the regularization parameter δ_n^2 is also larger so that the MR almost does not work in the MR-SOM. Fig. 4(a) shows that once δ_n^2 is gradually reduced to a smaller value, which is close to the threshold in [21], a better reconstructed result can be obtained. Consequently, from these results, the MR can work in the MR-SOM and achieve a better performance than the SOM only can obtain. The above numerical results provide strong evidence that the effect of the MR-SOM largely depends on the selection of the regularization parameter δ_n^2 , and it is greatly influenced by the level of noise. This fact requires that a suitable principle for the regularization should be given to make the algorithm more robust and stable, which is, however, not an easy task. In Section III, a new regularization principle is proposed in MR-FFT-TSOM. In fact, when all the Fourier bases in MR-FFT-TSOM are used, MR-FFT-TSOM is equivalent to MR-SOM. The following numerical results will show that MR-FFT-TSOM with the new regularization principle produces a quite stable result and is much less influenced by noise.

In the following, the performance of the MR-FFT-TSOM is examined using the same profile as above. Here, we choose $\alpha = 2/25$, which means that when $M_F = 7$, $\alpha(M_x/2 - M_F) = 2$. The reason to do so is just to choose a properly decreasing parameter δ_n^2 as optimization proceeds. Using the same synthetic data in MR-SOM, numerical results to evaluate the

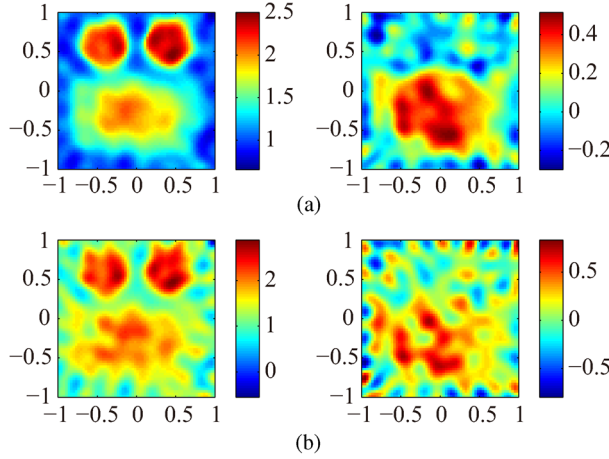


Fig. 4. Reconstruction results by MR-SOM with 30% AWGN, the (left) real and (right) imaginary part of the reconstruction relative permittivity ε_r when (a) $\delta_n^2 = \delta_{\text{CSI}}^2$ after 1000 iterations and (b) $\delta_n^2 = \delta_{\text{CSI}}^2 \times 2^3$ after 1500 iterations.

437 performance of the proposed MR-FFT-TSOM are presented.
438 First, 10% AWGN is added to the synthetic data. First, $M_F = 7$
439 and $M_F = 12$ are chosen for the reconstruction with the initial
440 guess being background. After one round of optimization with
441 750 iterations, the final reconstructed results for $M_F = 7$ and
442 $M_F = 12$ are shown in Figs. 5(a) and 6(a), respectively. We
443 see that the reconstructed results by MR-FFT-TSOM are much
444 better than that of MR-SOM. Moreover, compared with the
445 initial profile in Fig. 2, the imaginary part of the permittiv-
446 ity reconstructed with $M_F = 7$ is more accurate than $M_F =$
447 12, observed from the value in Figs. 5 and 6. However, the
448 profile reconstructed by $M_F = 12$ is more shaped-preserved
449 and differentiable than the one using $M_F = 7$, particularly
450 for the real part. These two figures further prove that small
451 values of M_F have higher capabilities for noise suppression;
452 nonetheless, large values of M_F show increased resolution for
453 the image reconstruction. The reason is that more high-order
454 components of the current subspace are considered so that we
455 can reconstruct an image with high resolution. Therefore, the
456 M_F balances the robustness against noise and the resolution
457 of the reconstruction. Moreover, when $\delta_n^2 = \delta_{\text{CSI}}^2$, the recon-
458 structed results when $M_F = 7$ and $M_F = 12$ can be obtained in
459 Figs. 5(b) and 6(b), respectively. Figs. 5(c) and 6(d) show δ_n^2 for
460 $M_F = 7$ and $M_F = 12$, respectively. The figures inside show
461 how δ_n^2 change after switching to the exponentially tunable
462 regularization and the corresponding $N_\kappa = 244, 220$. After the
463 changing point, the ratio between δ_{CSI}^2 and δ_n^2 is not large, i.e.,
464 about 4 on average. We see that when the noise level is 10%
465 AWGN, using $\delta_n^2 = \delta_{\text{CSI}}^2$ or δ_n^2 proposed in this paper, almost
466 the same reconstructed results can be obtained in MR-FFT-
467 TSOM. This is due to the fact that both principles are far less
468 than the produced $|\nabla \chi(\bar{r})|^2$, which means that when the noise
469 level is not high, the δ_{CSI}^2 is already enough. However, in the
470 following example, we will see that when the noise level is high,
471 there will be a difference between the two principles.

472 Before testing with the highly noisy data, we examine the
473 robustness of the proposed MR-FFT-TSOM compared with the
474 original FFT-TSOM. Fig. 6(c) shows the reconstruction result
475 obtained by successive multiple rounds of optimization by MR-
476 FFT-TSOM using $M_F = 5, M_F = 6$, and $M_F = 12$, with 300,

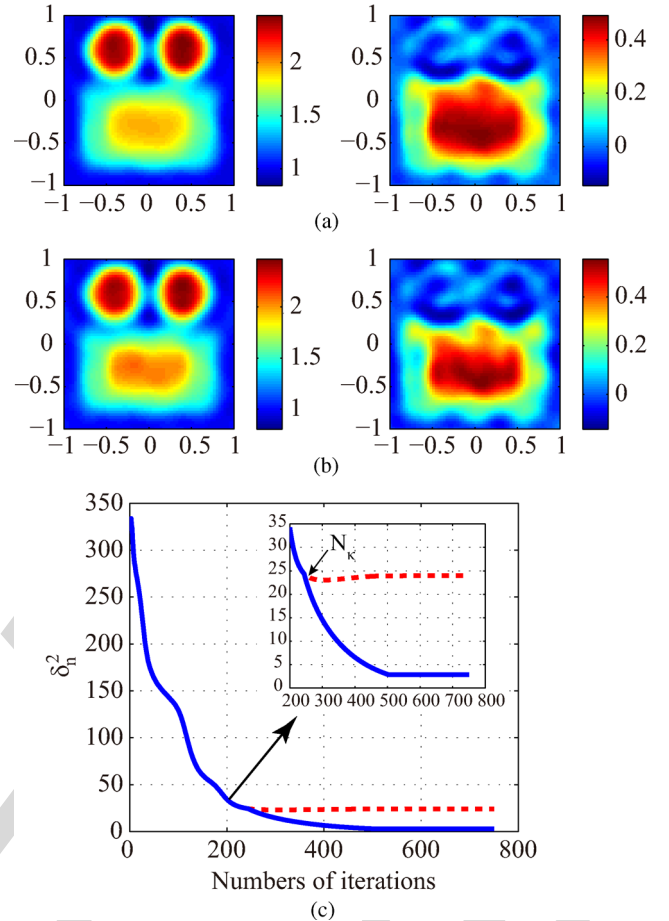


Fig. 5. Reconstruction results by MR-FFT-TSOM with 10% AWGN, the (left) real and (right) imaginary part of the reconstruction relative permittivity ε_r by (a) $M_F = 7$ after 750 iterations when $\delta_n^2 = \delta_{\text{CSI}}^2 \times e^{-((2/25)(32-M_F)(n-N_\kappa)/N_\kappa)}$ and (b) $M_F = 7$ after 750 iterations when $\delta_n^2 = \delta_{\text{CSI}}^2$. (c) δ_n^2 versus the iterations, $\delta_n^2 = \delta_{\text{CSI}}^2$ (dotted red line) and $\delta_n^2 = \delta_{\text{CSI}}^2 \times e^{-((2/25)(32-M_F)(n-N_\kappa)/N_\kappa)}$ (blue line). The figure inside illustrates the comparison from the switching point $N_\kappa = 244$.

300, and 150 iterations, respectively. The optimization results, 477 i.e., $\bar{\beta}_l$ and $\bar{\chi}$, obtained for the last iteration of the previous 478 round are set as the initial values to of the next round of opti- 479 mization. Here, we see that there is no improvement between 480 Fig. 6(a) and (c). Unlike FFT-TSOM [31], MR-FFT-TSOM 481 does not need to execute several rounds of optimization using 482 different numbers of the current subspace basis successively. 483 Furthermore, the proposed MR-FFT-TSOM has superior stabil- 484 ity and robustness compared with TSOM-based reconstruction 485 algorithms. 486

Second, we further investigate the performance of the MR- 487 FFT-TSOM with 30% AWGN added to the synthetic data. The 488 reconstruction results after 750 iterations by one round of opti- 489 mization under $M_F = 7$ and $M_F = 12$ are depicted in Fig. 7(a) 490 and (b), respectively. When the noise level is high, we see 491 that the reconstruct permittivity by $M_F = 7$ is more accurate 492 than by $M_F = 12$. Although the reconstructed profiles are a bit 493 distorted in Fig. 7, the results reconstructed by MR-FFT-TSOM 494 are better than that reconstructed by FFT-TSOM [31]. Because 495 MR-FFT-TSOM has twofold ability of the noise suppression, 496 not only TSOM but also the multiplicative regularization can 497 filter out the noise in the optimization procedure. When the 498

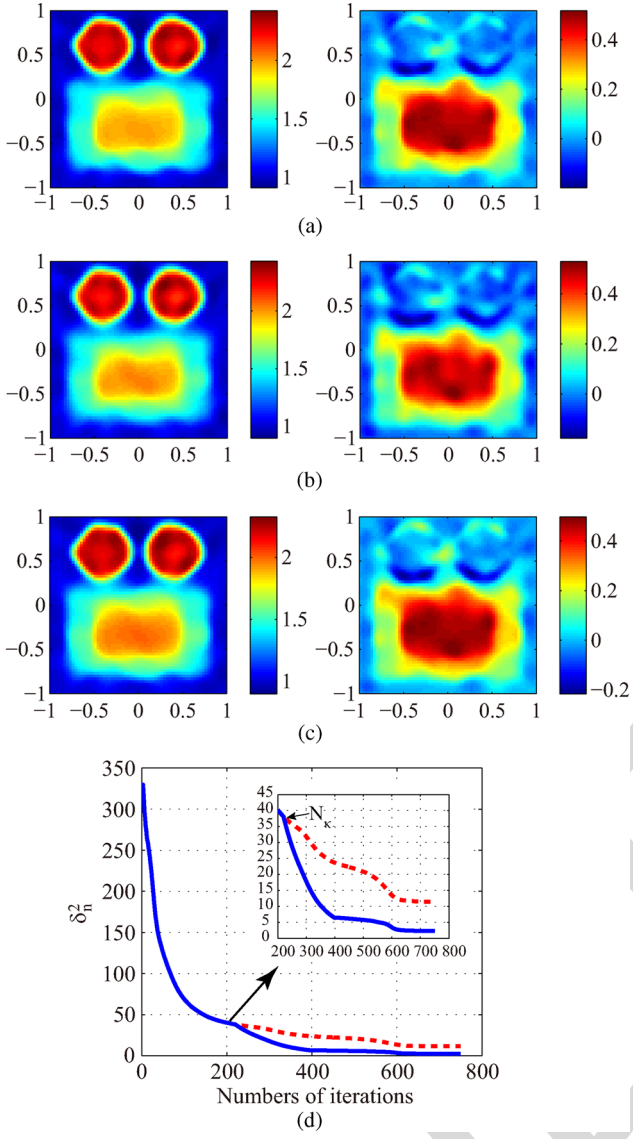


Fig. 6. Reconstruction results by MR-FFT-TSOM with 10% AWGN, the (left) real and (right) imaginary part of the reconstruction relative permittivity ε_r when (a) $M_F = 12$ and $\delta_n^2 = \delta_{CSI}^2 \times e^{-(2/25)(32-M_F)(n-N_\kappa)/N_\kappa}$ after 750 iterations and (b) $M_F = 12$ and $\delta_n^2 = \delta_{CSI}^2$ after 750 iterations. (c) Using three successive rounds of optimization, $M_F = 5$, $M_F = 6$, and $M_F = 12$ with 300, 300, and 150 iterations, respectively, when $\delta_n^2 = \delta_{CSI}^2 \times e^{-(2/25)(32-M_F)(n-N_\kappa)/N_\kappa}$. (d) δ_n^2 versus the iterations $M_F = 12$, $\delta_n^2 = \delta_{CSI}^2$ (dotted red line) and $\delta_n^2 = \delta_{CSI}^2 \times e^{-(2/25)(32-M_F)(n-N_\kappa)/N_\kappa}$ (blue line). The figure inside illustrates the comparison from the switching point $N_\kappa = 220$.

499 noise level is high, the residue of the field equation and the 500 gradient of the contrast will be large, and then, the noise will be 501 suppressed in the optimization procedure as mentioned in [21]. 502 Moreover, we also get the reconstructed results using $\delta_n^2 = \delta_{CSI}^2$ 503 under $M_F = 7$ and $M_F = 12$. When using $M_F = 7$, the two 504 principles show almost the same performance (the proposed 505 principle might give a slightly better result if one carefully 506 looks into the imaginary part of the reconstructed profile), as 507 shown in Fig. 7(a) and (c). This is mainly due to the strong 508 regularization effect of using a low dimension of the current 509 subspace. However, when using $M_F = 12$, which means that 510 the current subspace being used is no longer that low, one sees 511 that the result obtained with proposed principle, as depicted

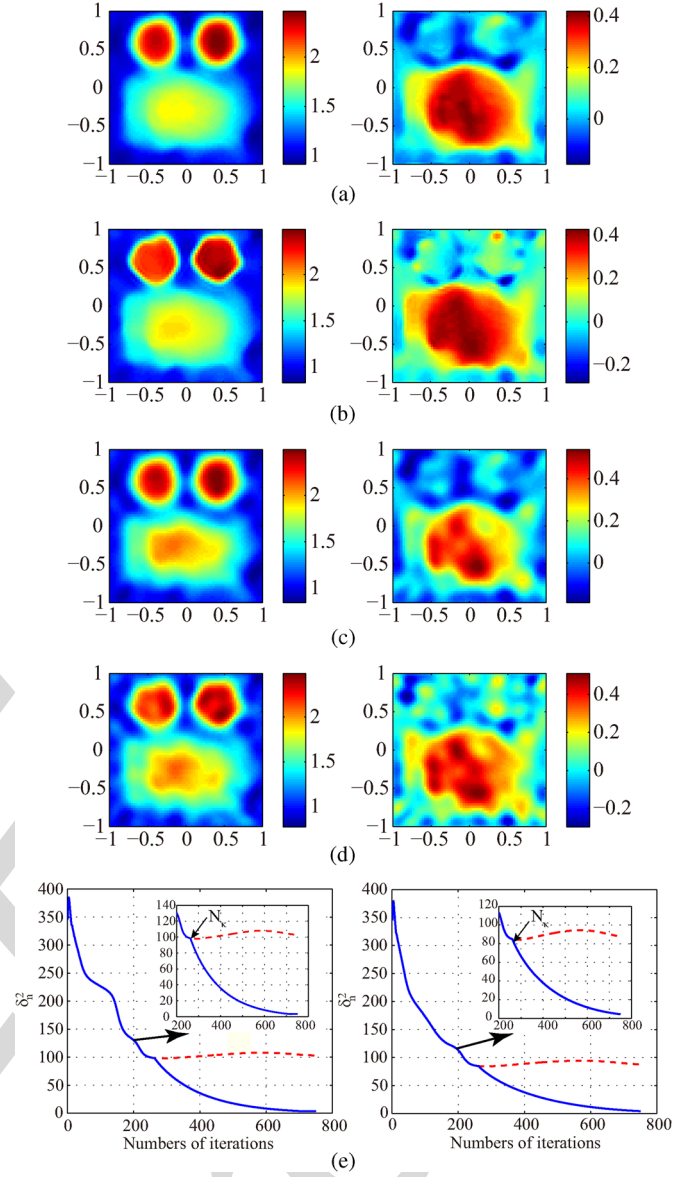


Fig. 7. Reconstruction results by MR-FFT-TSOM with 30% AWGN, the (left) real and (right) imaginary part of the reconstruction relative permittivity ε_r when (a) $M_F = 7$ and $\delta_n^2 = \delta_{CSI}^2 \times e^{-(2/25)(32-M_F)(n-N_\kappa)/N_\kappa}$ after 750 iterations; (b) $M_F = 12$ and $\delta_n^2 = \delta_{CSI}^2 \times e^{-(2/25)(32-M_F)(n-N_\kappa)/N_\kappa}$ after 750 iterations; (c) $M_F = 7$ and $\delta_n^2 = \delta_{CSI}^2$ after 750 iterations; (d) $M_F = 12$ and $\delta_n^2 = \delta_{CSI}^2$ after 750 iterations; (e) δ_n^2 versus the iterations, $\delta_n^2 = \delta_{CSI}^2$ (dotted red line) and $\delta_n^2 = \delta_{CSI}^2 \times e^{-(2/25)(32-M_F)(n-N_\kappa)/N_\kappa}$ (blue line), $M_F = 7$ (left) and $M_F = 12$ (right). The figures inside illustrate the comparison from the switching points $N_\kappa = 263, 261$, respectively.

in Fig. 7(b), is obviously better than the one with the CSI 513 principle, as depicted in Fig. 7(d). As shown in Fig. 7(e), the 513 numbers of switching points between δ_n^2 and δ_{CSI}^2 for $M_F = 514$ 7 and $M_F = 12$ are $N_\kappa = 263, 261$, respectively. After the 515 switching point, the ratio between δ_n^2 and δ_{CSI}^2 is large, i.e., 516 about 10 on average. This is due to the fact that the proposed 517 principle brings a stronger MR effect compared with the CSI 518 principle. Since one can obtain more information of the induced 519 current as well as the reconstructed profile when using a higher 520 dimension of the current subspace, the proposed principle is the 521 preferred principle being used in MR-FFT-TSOM. Therefore, 522

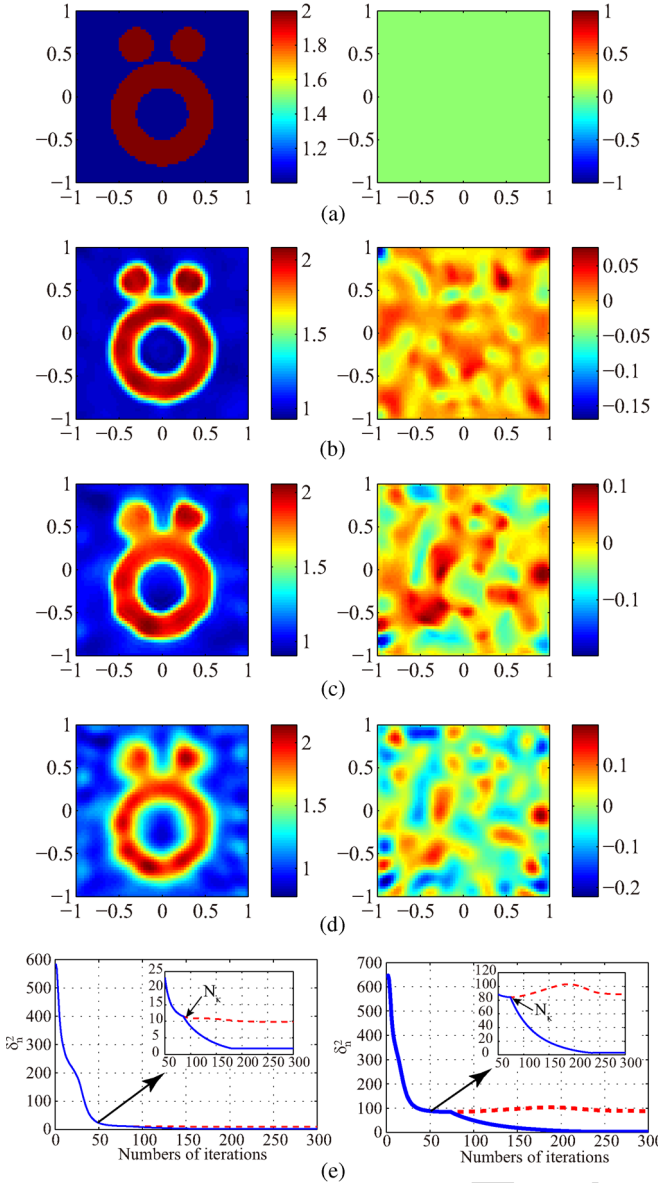


Fig. 8. (a) Exact Austria profile of DoI. Reconstruction result by the MR-FFT-TSOM after 300 iterations (b) when $M_F = 12$ and $\delta_n^2 = \delta_{\text{CSI}}^2 \times e^{-((2/25)(32-M_F)(n-N_\kappa)/N_\kappa)}$ with 10% AWGN; (c) when $M_F = 12$ and $\delta_n^2 = \delta_{\text{CSI}}^2 \times e^{-((2/25)(32-M_F)(n-N_\kappa)/N_\kappa)}$ with 30% AWGN; (d) when $M_F = 12$ and $\delta_n^2 = \delta_{\text{CSI}}^2$ with 30% AWGN; (e) δ_n^2 versus the iterations, $\delta_n^2 = \delta_{\text{CSI}}^2$ (dotted red line) and $\delta_n^2 = \delta_{\text{CSI}}^2 \times e^{-((2/25)(32-M_F)(n-N_\kappa)/N_\kappa)}$ (blue line), 10% AWGN (left) and 30% AWGN (right). The figures inside illustrate the comparison from the switching points $N_\kappa = 86, 74$, respectively.

we see that the proposed MR-FFT-TSOM not only inherits the merits of the FFT-TSOM but also holds the property of edge preserving in image restoration. Moreover, it is more stable and has better robustness against noise compared with FFT-TSOM. Above are the comparisons among MR-FFT-TSOM, MR-SOM, and FFT-TSOM by the inversion of the profile proposed in [31]. In the second case, we will further examine the effect of the proposed MR-FFT-TSOM by a classical and well-known Austria profile, which consists of an annular, two disks, and the background material [26]. The two disks are of the same 0.2-m radius, and their centers are $(-0.3, 0.6)$ m and $(0.3, 0.6)$ m. The annual is centered at $(0, -0.2)$ m with 0.3-m

inner radius and 0.6-m outer radius. All three scatters have the same relative permittivity $\varepsilon_r = 2$, as shown in Fig. 8(a). In this case, as previously mentioned, to keep the property of edge preserving, $M_F = 12$ is considered as the best choice for the Austria profile. The retrieval result after 300 iterations with 10% AWGN was shown in Fig. 8(b). We see that MR-FFT-TSOM gave a quite satisfactory result, which was quite close to the exact profile both in the shape of the profile or the accuracy of the permittivity. Further, we carried on the test to investigate the noise suppressions ability of the MR technique when the synthetic data are corrupted by 30% random additive white noise. In Fig. 8(c), we see that a satisfying reconstruction image after 300 iterations still can be obtained. As before, we also examine the performance of the MR-FFT-TSOM using $\delta_n^2 = \delta_{\text{CSI}}^2$ under 30% AWGN, which is shown in Fig. 8(d), where we see that the effect of edge preserving in MR is not such obvious. The numbers of switching points between δ_n^2 and δ_{CSI}^2 for 10% and 30% AWGN are $N_\kappa = 86, 74$, respectively, as shown in Fig. 8(e). Hence, the stability and effectiveness of the strategy of the regularization parameter δ_n^2 in the proposed MR-FFT-TSOM is further verified by various cases.

To further validate the proposed algorithm, MR-FFT-TSOM and FFT-TSOM were tested on the 2005 Fresnel data set [36]. Here, we present results from the *FoamTwinDiel* data set, which was collected for 18 transmitters, 241 receivers, and 9 frequencies from 2 to 10 GHz. The scatters, which consist of two smaller cylinders of relative permittivity $\varepsilon_r = 2$ with diameter = 3.1 cm where one of the smaller cylinders is embedded in a larger cylinder with $\varepsilon_r = 1.45$, diameter = 8 cm, are shown in Fig. 9(a). In the experimental case, a 45×45 grid mesh of the DoI, which is 15 cm \times 15 cm square centered at the origin, is used for the reconstruction. To calibrate the data, we make use of the method as outlined [36]. It is worth mentioning that all the numerical reconstructions are proceeded at a single frequency of 4 GHz instead of frequency hopping. According to the property of SVD of \bar{G}_S , $L = 10$ and $M_F = 12$ is considered as the choice for all the numerical simulation. The reconstructed results by the proposed MR-FFT-TSOM after 750 iterations are shown in Fig. 9(b). It is seen that the retrieval result exhibits an excellent effect of edge preserving and is quite satisfying. Similarly, the retrieval results after 750 iterations by FFT-TSOM and MR-FFT-TSOM when $\delta_n^2 = \delta_{\text{CSI}}^2$ are shown in Fig. 9(c) and (d), respectively. Fig. 9(e) shows δ_n^2 —iteration plot. The number of switching points between δ_n^2 and δ_{CSI}^2 is $N_\kappa = 86$. After the switching point, the ratio between δ_n^2 and δ_{CSI}^2 is more than 10. Although the results reconstructed by FFT-TSOM also can be a satisfying image, there is still not small disparity compared with the proposed MR-FFT-TSOM. Moreover, we can see that, only depending on data at a single frequency, MR-FFT-TSOM with $\delta_n^2 = \delta_{\text{CSI}}^2$ nearly could not reconstruct the satisfied image. However, as outlined in [37], significantly better results can be obtained with frequency-hopping inversion. Therefore, the proposed MR-FFT-TSOM exhibits excellent performance by both synthetic data and experimental data set. These figures reveal that the proposed MR-FFT-TSOM exhibit a better and more satisfying reconstruction effect compared with the results in SOM [26], TSOM [29], FFT-TSOM [31], and MR-SOM as well.

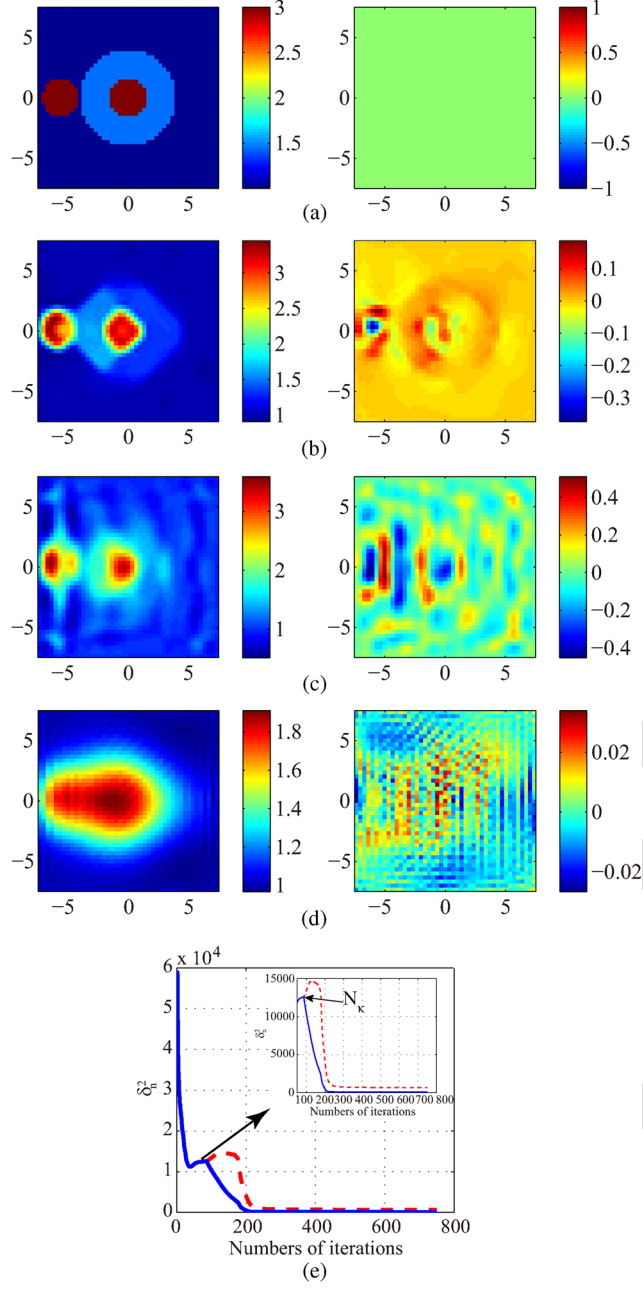


Fig. 9. Reconstruction of Fresnel data set *FoamTwinDiel*. (a) Exact profile of DOI. (b) Reconstruction result by the MR-FFT-TSOM using the proposed regularization parameter. (c) Reconstruction result by the FFT-TSOM. (d) Reconstruction result by the MR-FFT-TSOM when $\delta_n^2 = \delta_{\text{CSI}}^2$. (e) δ_n^2 versus the iterations, $\delta_n^2 = \delta_{\text{CSI}}^2$ (dotted red line) and $\delta_n^2 = \delta_{\text{CSI}}^2 \times e^{-((2/25)(32-M_F)(n-N_\kappa)/N_\kappa)}$ (blue line). The figure inside illustrates the comparison from the switching point $N_\kappa = 86$.

593

V. CONCLUSION

In this paper, we have proposed a new MR-FFT-TSOM for solving inverse scattering problems. In FFT-TSOM, the current subspace is spanned by discrete Fourier bases, and only the most influential bases are used. Based on the rule of the regularization parameter in MR-CSI, a modified and more stable and effective principle of the regularization parameter is put forward according to the property of the FFT-TSOM. The proposed MR-FFT-TSOM inherits the advantages of the FFT-TSOM earlier in [31], i.e., lower computational complexity

than the TSOM, better stability of the inversion procedure, and better robustness against noise compared with the SOM. Moreover, owing to the effect of the MR, the proposed MR-FFT-TSOM has twofold ability of noise suppression and the property of edge preserving, which outperform the FFT-TSOM. As can be seen from the numerical inversion results on both the synthetic data and experimental data shown in this paper and those in [26], [29], and [31], the performance of the MR-FFT-TSOM is superior to SOM, MR-SOM, TSOM, and FFT-TSOM. Although our experiments are set up for the 2-D TM case, it should be pointed out that the MR-FFT-TSOM can be readily extended to 2-D TE and 3-D cases as well.

REFERENCES

- [1] Y. Wang and W. Chew, "An iterative solution of the two-dimensional electromagnetic inverse scattering problem," *Int. J. Imag. Syst. Technol.*, vol. 1, no. 1, pp. 100–108, 1989.
- [2] W. Chew and Y. Wang, "Reconstruction of two-dimensional permittivity distribution using the distorted Born iterative method," *IEEE Trans. Med. Imag.*, vol. 9, no. 2, pp. 218–225, Jun. 1990.
- [3] Q. H. Liu *et al.*, "Active microwave imaging. I. 2-D forward and inverse scattering methods," *IEEE Trans. Microw. Theory Tech.*, vol. 50, no. 1, pp. 123–133, Jan. 2002.
- [4] L.-P. Song, C. Yu, and Q. H. Liu, "Through-Wall Imaging (TWI) by radar: 2-D tomographic results and analyses," *IEEE Trans. Geosci. Remote Sens.*, vol. 43, no. 12, pp. 2793–2798, Dec. 2005.
- [5] P. M. Van Den Berg and R. E. Kleinman, "A contrast source inversion method," *Inverse Problems*, vol. 13, no. 6, pp. 1607–1620, Dec. 1997.
- [6] P. M. van den Berg, A. Van Broekhoven, and A. Abubakar, "Extended contrast source inversion," *Inverse Problems*, vol. 15, no. 5, pp. 1325–1344, Oct. 1999.
- [7] P. Mojabi and J. LoVetri, "Overview and classification of some regularization techniques for the Gauss–Newton inversion method applied to inverse scattering problems," *IEEE Trans. Antennas Propag.*, vol. 57, no. 9, pp. 2658–2665, Sep. 2009.
- [8] P. Mojabi and J. LoVetri, "Microwave biomedical imaging using the multiplicative regularized Gauss–Newton inversion," *IEEE Antennas Wireless Propag. Lett.*, vol. 8, pp. 645–648, 2009.
- [9] P. Mojabi and J. LoVetri, "Comparison of TE and TM inversions in the framework of the Gauss–Newton method," *IEEE Trans. Antennas Propag.*, vol. 58, no. 4, pp. 1336–1348, Apr. 2010.
- [10] J. Li, H. Liu, and J. Zou, "Multilevel linear sampling method for inverse scattering problems," *SIAM J. Sci. Comput.*, vol. 30, no. 3, pp. 1228–1250, 2008.
- [11] M. Pastorino, "Stochastic optimization methods applied to microwave imaging: A review," *IEEE Trans. Antennas Propag.*, vol. 55, no. 3, pp. 538–548, Mar. 2007.
- [12] P. Rocca, M. Benedetti, M. Donelli, D. Franceschini, and A. Massa, "Evolutionary optimization as applied to inverse scattering problems," *Inverse Problems*, vol. 25, no. 12, pp. 123 003-1–123 003-41, Dec. 2009.
- [13] C.-H. Huang, C.-C. Chiu, C.-L. Li, and K.-C. Chen, "Time domain inverse scattering of a two-dimensional homogenous dielectric object with arbitrary shape by particle swarm optimization," *Progr. Electromagn. Res.*, vol. 82, pp. 381–400, 2008.
- [14] T. Isernia, L. Crocco, and M. D'Urso, "New tools and series for forward and inverse scattering problems in lossy media," *IEEE Geosci. Remote Sens. Lett.*, vol. 1, no. 4, pp. 327–331, Oct. 2004.
- [15] L. Crocco, M. D'Urso, and T. Isernia, "Testing the contrast source extended Born inversion method against real data: The TM case," *Inverse Problems*, vol. 21, no. 6, pp. S33–S50, Dec. 2005.
- [16] I. Catapano, L. Crocco, M. D'Urso, and T. Isernia, "A novel effective model for solving 3-D nonlinear inverse scattering problems in lossy scenarios," *IEEE Geosci. Remote Sens. Lett.*, vol. 3, no. 3, pp. 302–306, Jul. 2006.
- [17] I. Catapano, L. Crocco, M. D'Urso, and T. Isernia, "3D microwave imaging via preliminary support reconstruction: Testing on the Fresnel 2008 database," *Inverse Problems*, vol. 25, no. 2, pp. 024002-1–024002-23, Feb. 2009.
- [18] M. D'Urso, T. Isernia, and A. F. Morabito, "On the solution of 2-D inverse scattering problems via source-type integral equations," *IEEE Trans. Geosci. Remote Sens.*, vol. 48, no. 3, pp. 1186–1198, Mar. 2010.

- 673 [19] A. Abubakar, P. M. Van den Berg, and J. J. Mallorqui, "Imaging of
674 biomedical data using a multiplicative regularized contrast source inver-
675 sion method," *IEEE Trans. Microw. Theory Tech.*, vol. 50, no. 7, pp. 1761–
676 1771, Jul. 2002.
677 [20] P. Abubakar, "Contrast source inversion method: State of art," *Prog.
678 Electromagn. Res.*, vol. 34, pp. 189–218, 2001.
679 [21] P. M. van den Berg, A. Abubakar, and J. T. Fokkema, "Multiplicative
680 regularization for contrast profile inversion," *Radio Sci.*, vol. 38, no. 2,
681 pp. 231–23–10, Apr. 2003.
682 [22] A. Abubaker and P. M. Van Den Berg, "Total variation as a multiplicative
683 constraint for solving inverse problems," *IEEE Trans. Image Process.*,
684 vol. 10, no. 9, pp. 1384–1392, Sep. 2001.
685 [23] A. Abubakar, P. M. Van Den Berg, T. M. Habashy, and H. Braunsch,
686 "A multiplicative regularization approach for deblurring problems," *IEEE
687 Trans. Image Process.*, vol. 13, no. 11, pp. 1524–1532, Nov. 2004.
688 [24] X. Chen, "Application of signal-subspace and optimization methods in
689 reconstructing extended scatterers," *J. Opt. Soc. Amer. A*, vol. 26, no. 4,
690 pp. 1022–1026, Apr. 2009.
691 [25] X. Ye, Y. Zhong, and X. Chen, "Reconstructing perfectly electric con-
692 ductors by the subspace-based optimization method with continuous
693 variables," *Inverse Problems*, vol. 27, no. 5, pp. 055011–1–055011–14,
694 May 2011.
695 [26] X. Chen, "Subspace-based optimization method for solving inverse-
696 scattering problems," *IEEE Trans. Geosci. Remote Sens.*, vol. 48, no. 1,
697 pp. 42–49, Jan. 2010.
698 [27] Y. Zhong, X. Chen, and K. Agarwal, "An improved subspace-based op-
699 timization method and its implementation in solving three-dimensional
700 inverse problems," *IEEE Trans. Geosci. Remote Sens.*, vol. 48, no. 10,
701 pp. 3763–3768, Oct. 2010.
702 [28] X. Ye, X. Chen, Y. Zhong, and R. Song, "Simultaneous reconstruction of
703 dielectric and perfectly conducting scatterers via T-matrix method," *IEEE
704 Trans. Antennas Propag.*, vol. 61, no. 7, pp. 3774–3781, Jul. 2013.
705 [29] Y. Zhong and X. Chen, "Twofold subspace-based optimization method
706 for solving inverse scattering problems," *Inverse Problems*, vol. 25, no. 8,
707 pp. 085003–1–085003–11, Aug. 2009.
708 [30] Y. Zhong, "Subspace-based inversion methods for solving electromagnetic
709 inverse scattering problems," Ph.D. dissertation, Nat. Univ. Singa-
710 pore, Singapore, 2010.
711 [31] Y. Zhong and X. Chen, "An FFT twofold subspace-based optimization
712 method for solving electromagnetic inverse scattering problems," *IEEE
713 Trans. Antennas Propag.*, vol. 59, no. 3, pp. 914–927, Mar. 2011.
714 [32] T. Isernia, V. Pascazio, and R. Pierri, "A nonlinear estimation method in
715 tomographic imaging," *IEEE Trans. Geosci. Remote Sens.*, vol. 35, no. 4,
716 pp. 910–923, Jul. 1997.
717 [33] O. M. Bucci, L. Crocco, T. Isernia, and V. Pascazio, "Inverse scatter-
718 ing problems with multifrequency data: Reconstruction capabilities and
719 solution strategies," *IEEE Trans. Geosci. Remote Sens.*, vol. 38, no. 4,
720 pp. 1749–1756, Jul. 2000.
721 [34] R. Pierri, G. Rubinacci, A. Tamburino, S. Ventre, and F. Villone, "Non-
722 linear inverse resistivity profiling using wavelets," *IEEE Trans. Magn.*,
723 vol. 34, no. 5, pp. 2920–2923, Sep. 1998.
724 [35] P. Van den Berg and R. Kleinman, "A total variation enhanced modified
725 gradient algorithm for profile reconstruction," *Inverse Problems*, vol. 11,
726 no. 3, pp. L5–L10, Jun. 1995.
727 [36] J.-M. Geffrin, P. Sabouroux, and C. Eyraud, "Free space experimental
728 scattering database continuation: Experimental set-up and measurement
729 precision," *Inverse Problems*, vol. 21, no. 6, pp. S117–S130, Dec. 2005.
730 [37] R. F. Bloemenkamp, A. Abubakar, and P. M. van den Berg, "Inversion
731 of experimental multi-frequency data using the contrast source inversion
732 method," *Inverse Problems*, vol. 17, no. 6, pp. 1611–1622, Dec. 2001.

Kuiwen Xu received the B.S. degree from Hangzhou Dianzi University, Hangzhou, China, in 2009. He is currently working toward the Ph.D. degree in the Laboratory of Applied Research on Electromagnetics, Zhejiang University, Hangzhou.

During 2012–2013, he was a Visiting Scholar with the National University of Singapore, Singapore. His recent research interests include microwave circuit, array antennas, and inverse scattering problems.



Yu Zhong was born in Guangdong, China, in 1980. 742 He received the B.S. and M.S. degrees in electronic 743 engineering from Zhejiang University, Hangzhou, 744 China, in 2003 and 2006, respectively, and the Ph.D. 745 degree from the National University of Singapore, 746 Singapore, in 2010. 747

He is currently a Scientist with the Institu- 748 tion of High Performance Computing, A*STAR, 749 Singapore. In 2012 and 2013, he was an Invited 750 Senior Scientific Expert with the Laboratoire des 751 Signaux et Systèmes, Gif-sur-Yvette, France. His 752 research interests include inverse scattering problems and electromagnetic 753 modeling on composite materials. 754



Rencheng Song received the B.S. degree in 755 computational mathematics from Jilin University, 756 Changchun, China, in 2005 and the Ph.D. de- 757 gree from Zhejiang University, Hangzhou, China, 758 in 2010. 759

From July 2010 to January 2013, he was with the 760 Department of Electrical and Computer Engineering, 761 National University of Singapore, Singapore. He is 762 currently a Principal Scientist with Halliburton Far 763 East Pte. Ltd., Singapore. His research interests in- 764 clude electromagnetic inverse problems, particularly 765 well-logging applications. 766



Xudong Chen (M'09) received the B.S. and M.S. 767 degrees in electrical engineering from Zhejiang Uni- 768 versity, Hangzhou, China, in 1999 and 2001, respec- 769 tively, and the Ph.D. degree from the Massachusetts 770 Institute of Technology, Cambridge, MA, USA, 771 in 2005. 772

Since then, he joined the Department of Electrical 773 and Computer Engineering, National University of 774 Singapore, Singapore, where he is currently an As- 775 sociate Professor. In 2010, he was an invited Visiting 776 Associate Professor with the University of Paris- 777 SUD 11. During 2012–2013, he took a sabbatical leave at Stanford University, 778 Stanford, CA, USA, where he worked on microwave impedance tomography. 779 He has published more than 100 journal papers on inverse scattering problems, 780 material parameter retrieval, and optimization algorithms. His research interests 781 mainly include electromagnetic inverse problems. 782

Dr. Chen was the recipient of the Young Scientist Award by the Union Radio- 783 Scientifique Internationale in 2010. 784



Lixin Ran received the B.S., M.S., and Ph.D. de- 785 grees from Zhejiang University, Hangzhou, China, in 786 1991, 1994, and 1997, respectively. 787

In 1997, he became an Assistant Professor; in 788 1999, an Associate Professor; and in 2004, a Full 789 Professor with the Department of Information and 790 Electronics Engineering, Zhejiang University. He is 791 currently the Director of the Laboratory of Applied 792 Research on Electromagnetics (ARE), Zhejiang Uni- 793 versity. In 2005, 2009, and 2012, he was a Visiting 794 Scientist with the Massachusetts Institute of Tech- 795

nology, Cambridge, MA, USA. He has coauthored over 120 research papers 796 published in peer-reviewed journals. He holds over 30 patents. His research 797 interests include new concept antennas; radio-aware sensing and imaging; radio 798 frequency, microwave, and terahertz systems; and artificial active media. 799

AUTHOR QUERIES

AUTHOR PLEASE ANSWER ALL QUERIES

Please be aware that authors are required to pay overlength page charges (\$200 per page) if the paper is longer than 6 pages. If you cannot pay any or all of these charges please let us know.

This pdf contains 2 proofs. The first half is the version that will appear on Xplore. The second half is the version that will appear in print. If you have any figures to print in color, they will be in color in both proofs.

The “Open Access” option for your paper expires when the paper is published on Xplore in an issue with page numbers. Papers in “Early Access” may be changed to Open Access.

AQ1 = Note that Fig. 2 was uncited in the original text. Please check if the suggested text citation for Fig. 2 is appropriate. Otherwise, kindly provide the necessary corrections.

AQ2 = Please provide issue number and month of publication.

END OF ALL QUERIES

IEEE Proof

Multiplicative-Regularized FFT Twofold Subspace-Based Optimization Method for Inverse Scattering Problems

Kuiwen Xu, Yu Zhong, Rencheng Song, Xudong Chen, *Member, IEEE*, and Lixin Ran

Abstract—In this paper, we combine two techniques together, i.e., the fast Fourier transform-twofold subspace-based optimization method (FFT-TSOM) and multiplicative regularization (MR) to solve inverse scattering problems. When applying MR to the objective function in the FFT-TSOM, the new method is referred to as MR-FFT-TSOM. In MR-FFT-TSOM, a new stable and effective strategy of regularization has been proposed. MR-FFT-TSOM inherits not only the advantages of the FFT-TSOM, i.e., lower computational complexity than the TSOM, better stability of the inversion procedure, and better robustness against noise compared with the SOM, but also the edge-preserving ability from the MR. In addition, a more relaxed condition of choosing the number of current bases being used in the optimization can be obtained compared with the FFT-TSOM. Particularly, MR-FFT-TSOM has even better robustness against noise compared with the FFT-TSOM and multiplicative regularized contrast source inversion (MR-CSI). Numerical simulations including both inversion of synthetic data and experimental data from the Fresnel data set validate the efficacy of the proposed algorithm.

Index Terms—Fast Fourier transform-twofold subspace-based optimization method (FFT-TSOM), inverse scattering, multiplicative regularization (MR), optimization, subspace.

27

I. INTRODUCTION

INVERSE scattering problems have been of interest for many years, the same being widely applied in medical imaging, geophysics, biological studies, nondestructive testing and evaluation, through-wall imaging, etc. The goal of the inversion mainly considers the reconstruction of the location, the shape, the quantity, and the electric constitutive parameters of unknown objects inside a bounded domain of interest (DoI) immersed in a known background medium including, i.e., permittivity and conductivity, when the object is illuminated by a series of known incident electromagnetic waves.

Manuscript received June 19, 2013; revised December 11, 2013, March 25, 2014, and May 24, 2014; accepted May 29, 2014. This work was supported in part by the Singapore Temasek Defence Systems Institute under Grant TDSI/11-010/1A and in part by Institute Fresnel and the National Natural Science Foundation of China under Grant 61131002 and Grant 61071063.

K. Xu and L. Ran are with the Laboratory of Applied Research on Electromagnetics (ARE), Zhejiang University, Hangzhou 310027, China (e-mail: kuiwenxu@gmail.com; ranlx@zju.edu.cn).

Y. Zhong is with the A*STAR, Institution of High Performance Computing, Singapore 138632 (e-mail: zhongyu@ihpc.a-star.edu.sg).

R. Song and X. Chen are with the Department of Electrical and Computer Engineering, National University of Singapore, Singapore 117576 (e-mail: elezhong@nus.edu.sg; dr.csong@gmail.com; elechenx@nus.edu.sg).

Color versions of one or more of the figures in this paper are available online at <http://ieeexplore.ieee.org>.

Digital Object Identifier 10.1109/TGRS.2014.2329032

To deal with intrinsical nonlinearity and ill-posedness, many iterative algorithms have been proposed so far, such as the Born iterative method [1], the distorted Born iterative method [2]–[4], the contrast source inversion (CSI) method [5], [6], Gauss–Newton-type methods [7]–[9], the multilevel linear sampling method [10], and other stochastic type of inversion methods such as the genetic algorithm and the evolutionary algorithm [11]–[13]. Moreover, recently, to reduce the degree of nonlinearity of the relationship among the data and the unknowns, as well as the overall computational burden, the contrast-source-extended Born inversion methods are quickly exploited [14]–[18]. Indeed, these works have shed some light on the territory of how the most difficult inverse scattering problems can be solved. In most of the aforementioned algorithms, regularization techniques are applied so as to stabilize the solvers. These regularization techniques are mainly proposed from a mathematical point of view, such as the Tikhonov regularization, minimization of total variation, and so on. Particularly, van den Berg *et al.* investigated a multiplicative form total variation regularization together with the CSI, i.e., the multiplicative regularized contrast source inversion (MR-CSI) technique [6], [19]–[23]. Using the L_1 - and L_2 -norm total variation, where the weighting parameter is prescribed by the error norm of the original objective function in CSI so as to avoid the uncertainty and unpredictability of the weighting parameters [6], [21], the MR-CSI obtains quite satisfactory results with preserving edges of shapes of unknown scatters.

Recently, a subspace-based optimization method (SOM) has been proposed for reconstructing the dielectric profile of scatterers from scattered fields in both 2-D and 3-D electromagnetic inverse scattering problems [24]–[28]. The SOM utilizes the spectral property of the mapping from the induced current to measured scattered fields and determines part of the induced current in the DoI and obtains the remaining part of the induced current by the optimization. By doing so, the SOM only searches the solution within a subspace of the whole current space and, thus, stabilizes the solution to some extent. Given the SOM, a twofold SOM (TSOM) is further proposed to utilize the spectral property of the mapping from the induced current to the scattered fields in the DoI [29], [30], in which the remaining parts of the induced current are constructed using a new set of orthogonal basis according to their influence on the fields inside the DoI. By choosing a small number of bases, the optimization problem therein is simplified owing to the current subspace used with only the most influential bases and, thus,

83 with much smaller dimensions than the one used in the SOM.
 84 Given a good approximation to the original physical modeling
 85 and much smaller number of unknowns, the TSOM achieves
 86 better stability and better robustness against noise compared
 87 with the SOM.

88 In the TSOM, to obtain the spectral information of the map-
 89 ping from the current to the fields inside the domain, singular
 90 value decomposition (SVD) of the mapping is needed, which
 91 might cost a lot of computational resources when the problem
 92 is not a small-scale one. To further accelerate the optimization
 93 and avoid the computationally burdensome SVD, a fast Fourier
 94 transform (FFT) TSOM has been proposed by using the current
 95 subspace constructed by discrete Fourier bases that is a good
 96 approximation to the original current subspace spanned by sin-
 97 gular vectors [31]. In the aforementioned literatures, the FFTs
 98 are usually solely used as an acceleration of the multiplication
 99 of Green's function and the induced current. Moreover, the
 100 Fourier bases are used to represent the dielectric profile as
 101 well [32]–[34]. However, though it might reduce the number
 102 of unknowns a bit, such a representation of the profile does not
 103 help much on addressing the ill-posedness and nonlinearity of
 104 the problem. Our use of the Fourier bases in FFT-TSOM is on
 105 constructing the induced current. Moreover, the FFT-TSOM not
 106 only inherits the merits of TSOM including better stability and
 107 better robustness against noise compared with the SOM but also
 108 dramatically reduces the computational complexity compared
 109 with the TSOM. To obtain the best stability of the solver, both
 110 the FFT-TSOM and the TSOM need to gradually increase the
 111 number of bases in different phase of the optimization. Such
 112 a lower-dimension technique for the current subspace can be
 113 considered as a physical regularization, which is different from
 114 those aforementioned mathematical regularizations.

115 Due to the fact that they are different types of regulariza-
 116 tion techniques, in this paper, we combine the two techniques
 117 together, i.e., the FFT-TSOM and multiplicative regularization
 118 (MR). The purpose of doing so is to propose a new com-
 119 pound regularization technique that outperforms the original
 120 two methods with better robustness against noise. Due to the
 121 difference between the FFT-TSOM and the CSI, when applying
 122 the MR to the objective function in FFT-TSOM, one needs to
 123 adjust the MR parameter accordingly, which will be discussed
 124 in detail in this paper. After applying the MR technique to
 125 the FFT-TSOM, the new method, which is referred to as MR-
 126 FFT-TSOM, is tested with different dielectric profiles, and the
 127 numerical results show that the MR-FFT-TSOM presents some
 128 new properties: 1) As expected, the MR-FFT-TSOM preserves
 129 the advantages of the original FFT-TSOM, i.e., better stability
 130 and robustness against noise compared with the original SOM
 131 and MR-CSI, and also inherits the edge-preserving ability from
 132 the MR; 2) after introducing the MR, the MR-FFT-TSOM has a
 133 more relaxed condition of choosing the number of current bases
 134 being used in the optimization compared with the FFT-TSOM,
 135 which makes MR-FFT-TSOM easier to implement; 3) the new
 136 MR-FFT-TSOM has even better robustness against noise com-
 137 pared with the FFT-TSOM and MR-CSI; 4) a new strategy of
 138 the regularization parameter has been proposed and makes MR-
 139 FFT-TSOM more robust and stable. The give properties have
 140 been tested by noisy synthetic data and the Fresnel data set.

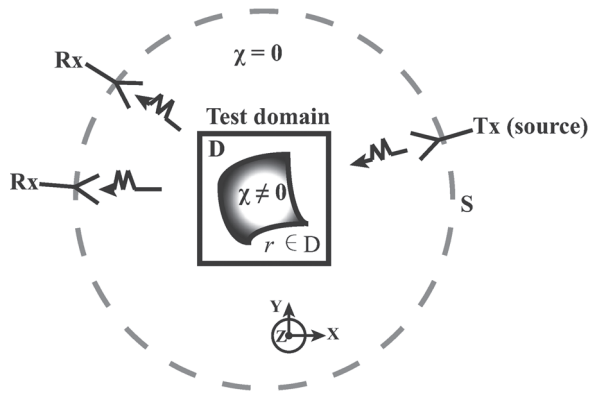


Fig. 1. Basic geometrical model of the inverse scattering problem.

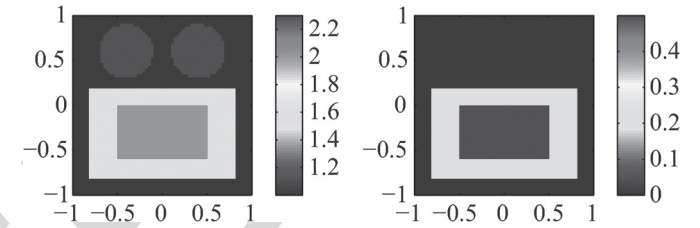


Fig. 2. Exact profile mentioned in [31], the (left) real and (right) imaginary part of the relative permittivity ϵ_r .

II. FORMULATION OF THE PROBLEM

141

Here, a 2-D electromagnetic inverse scattering problem with 142 the transverse magnetic (TM) incidence is considered. The 143 model of the 2-D inverse scattering problems consists of a 144 bounded DoI $D(D \subset \mathbb{R}^2)$, where nonmagnetic scatterers are 145 located with unknown permittivity $\epsilon(\bar{r}), \bar{r} \in D$, and the back- 146 ground homogeneous medium with permittivity ϵ_b , permeabil- 147 ity μ_b , and wavenumber $k_b = \omega/\sqrt{\epsilon_b\mu_b}$, $\mu_b = \mu_0$. Let us say 148 there are a total of N_i incidences from line sources at a single 149 frequency located at $\bar{r}_l^i, l = 1, 2, \dots, N_i$ in the domain (or on 150 curve) S outside of D , and these incident fields are denoted 151 as \bar{E}_l^{inc} . For each incidence, the scattered electric fields are 152 measured by N_r antennas located at $r_q^s, q = 1, 2, \dots, N_r$, as 153 depicted in Fig. 1. The complex contrast in the DoI is defined 154 as $\chi(\bar{r}) = (\epsilon(\bar{r}) - \epsilon_b)/\epsilon_b$. In the inverse problem, we need to 155 determine $\epsilon(\bar{r})$, given a set of $N_i N_r$ scattering data, \bar{E}_l^{sca} . The 156 test domain D in the $x - y$ plane is discretized into many small 157 rectangular subdomains with a smaller than 1/10 wavelength 158 dimension and centered at \bar{r}_m . The total number of subdomains 159 is M . In this paper, the domains of interest are chosen to be 160 rectangular to implement the conjugate gradient fast Fourier 161 transform (CG-FFT) scheme and apply the FFT algorithm with 162 the new Fourier bases (see Fig. 2).

163 AQ1

What follows is a quick review of the FFT-TSOM, and more 164 details can be found in [31]. The method of moments (MoM) is 165 used to discretize the original Lippmann–Schwinger equation. 166 For the l th incidence, the total electric field at the center of the 167 m th subunit $\bar{E}_{l;m}^{\text{tot}}$ is given by

$$\bar{E}_{l;m}^{\text{tot}} = \bar{E}_{l;m}^{\text{inc}} + \sum_{n=1}^M \bar{G}_D(\bar{r}_m, \bar{r}_n) \cdot \bar{I}_{l;n}, \quad m = 1, 2, \dots, M \quad (1)$$

169 where $\bar{E}_{l;n}^{\text{inc}}$ is the incident electric field at \bar{r}_m , and $\bar{I}_{l;n}$ is the
170 induced current at \bar{r}_n , which can be related to the total electric
171 filed $\bar{E}_{l;n}^{\text{tot}}$ by

$$\bar{I}_{l;n} = -i\omega\epsilon_b\chi_n \bar{E}_{l;n}^{\text{tot}}, \quad n = 1, 2, \dots, M. \quad (2)$$

172 $\bar{G}_D(\bar{r}_m, \bar{r}_n)$ denotes the Green function of the background
173 media.

174 It is convenient to write (1) and (2) in compact form as

$$\bar{I}_l = -i\omega\epsilon_b\bar{\chi} \cdot (\bar{E}_l^{\text{inc}} + \bar{G}_D \cdot \bar{I}_l) \quad (3)$$

175 where $\bar{I}_l = [I_{l;1}(r_1), I_{l;2}(r_2), \dots, I_{l;M}(r_M)]^T$ is an M -
176 dimensional vector, i.e., $\bar{E}_l^{\text{inc}} = [E_{l;1}^{\text{inc}}, E_{l;2}^{\text{inc}}, \dots, E_{l;M}^{\text{inc}}]^T$, and
177 superscript T denotes the transpose operator.

178 The integral operator relating the induced current and the
179 scattered fields can be expressed as

$$\bar{E}_l^{\text{sca}} = \bar{G}_S \cdot \bar{I}_l, \quad l = 1, 2, \dots, N_i \quad (4)$$

180 where $\bar{E}_l^{\text{sca}} = [E_l^{\text{sca}}(r_1^s), E_l^{\text{sca}}(r_2^s), \dots, E_l^{\text{sca}}(r_{N_r}^s)]^T$, \bar{G}_S is an
181 $N_r \times M$ matrix with elements $\bar{G}_S(\bar{r}_q^s, \bar{r}_m)$ being Green's func-
182 tion from the DoI to the measurement. Equations (3) and (4)
183 are considered as the current equation and the field equation,
184 respectively (or the state equation and the data equation referred
185 to in [26]).

186 From [26], with the spectral information from the SVD of
187 $\bar{G}_S(\bar{G}_S \cdot \bar{v}_j^S = \sigma_j^S \bar{u}_j^S)$, the induced current is split into two parts
188 in the SOM, i.e., the deterministic portion and the ambiguous
189 part, the former of which can be obtained by

$$\bar{I}_l^d = \sum_{j=1}^L \bar{u}_j \frac{\bar{v}_j^S}{\sigma_j^S} \bar{v}_j^S = \bar{V}_S^+ \cdot \bar{\alpha}_l^+ \quad (5)$$

190 where $\bar{V}_S^+ = [\bar{v}_1^S, \bar{v}_2^S, \dots, \bar{v}_L^S]$, and $\bar{\alpha}_l^+ = [\alpha_{l;1}^+, \alpha_{l;2}^+, \dots,
191 \alpha_{l;L}^+]^T$, $\alpha_{l;j}^+ = (\bar{u}_j^S \cdot \bar{E}_l^{\text{sca}})/\sigma_j^S, j = 1, 2, \dots, L$, superscript *
192 denotes the Hermitian operation, whereas superscript + refers
193 to the dominant current space, the subspace corresponding
194 to the dominant singular values. The value of L is chosen
195 according to the singular values of \bar{G}_S and the level of noise
196 [24], [26]. On the other hand, as mentioned in the TSOM [29],
197 we can express the ambiguous part of the induced current as

$$\bar{I}_l^a(\bar{\beta}_l) = \bar{V}_D^+ \cdot \bar{\beta}_l \quad (6)$$

198 where $\bar{\beta}_l$ is an M_0 -dimensional vector, and the corresponding
199 current subspace \bar{V}_D^+ can be expressed as

$$\bar{V}_D^+ = \left(\bar{I}_M - \bar{V}_S^+ \cdot \bar{V}_S^{+*} \right) \cdot \bar{V}_D^+ \quad (7)$$

200 where $\bar{V}_D^+ = [\bar{v}_1^D, \bar{v}_2^D, \dots, \bar{v}_{M_0}^D]$ is the current subspace
201 spanned by the singular vectors to the largest M_0 singular
202 values of the operator \bar{G}_D [29], [30]. However, to avoid the
203 computational burdensome SVD of the operator \bar{G}_D and further
204 accelerate the process of optimization, the original current sub-
205 space spanned by the singular vector bases can be substituted

206 by the discrete Fourier bases such that the FFT-TSOM was
207 proposed in [31]. Thus

$$\begin{aligned} \bar{I}_l^a &= \left(\bar{I}_M - \bar{V}_S^+ \cdot \bar{V}_S^{+*} \right) \cdot [\bar{F}_1^D, \bar{F}_2^D, \dots, \bar{F}_{M_0}^D] \cdot \bar{\beta}_l \\ &= \left(\bar{I}_M - \bar{V}_S^+ \cdot \bar{V}_S^{+*} \right) \cdot \text{vec}\{\text{IDFT}\{\bar{\gamma}_l\}\} \end{aligned} \quad (8)$$

208 where $\bar{F}_j, j = 1, 2, \dots, M_0$ are the vectorized discrete Fourier
209 bases, and $\bar{\gamma}_l$ is the 2-D Fourier coefficient tensor with nonzero
210 elements corresponding to those low-frequency discrete Fourier
211 bases (denoted as four blocks with size M_F in the four cor-
212ners of the coefficient tensor in MATLAB) and zero elements
213 corresponding to the remaining high-frequency discrete Fourier
214 bases. The $\text{vec}\{\cdot\}$ is the vectorization operator. As mentioned
215 in [31], low-frequency Fourier bases can be used to construct a
216 current subspace as the approximation to the original current
217 subspace spanned by the singular vectors with large singu-
218 lar values. The inverse discrete Fourier transform (IDFT) is
219 performed by the 2-D FFT algorithm, and the computational
220 complexity is $O(M \log_2 M)$, which is much smaller than the
221 one of the direct multiplication in the TSOM. Detail of the FFT-
222 TSOM could be found in [31].

223 After constructing the induced current in the aforementioned
224 way, the objective function is defined as below. First, the
225 mismatch of the scattered fields is defined as

$$\Delta_l^{\text{fe}}(\bar{\beta}_l) = \|\bar{G}_S \cdot \bar{I}_l^a + \bar{G}_S \cdot \bar{I}_l^d - \bar{E}_l^{\text{sca}}\|^2 \quad (9)$$

226 where $\|\cdot\|$ is the Euclidean length of a vector. Similarly, the
227 current equation is another key equation to satisfy. The residue
228 in the current equation is defined to be [31]

$$\Delta_l^{\text{cur}}(\bar{\beta}_l, \bar{\chi}) = \|\bar{\mathcal{L}}_{\text{SOM}}(\bar{\beta}_l) - \bar{\Gamma}_l\|^2 \quad (10)$$

229 where $\bar{\mathcal{L}}_{\text{SOM}}(\bar{\beta}_l) = (\bar{I}_l^a(\bar{\beta}_l)/-i\omega\epsilon_b) - \bar{\chi}\bar{G}_D \cdot \bar{I}_l^a(\bar{\beta}_l)$, and $\bar{\Gamma}_l = 229$
230 $\bar{\chi}(\bar{E}_l^{\text{inc}} + \bar{G}_D \cdot \bar{I}_l^d) + \bar{I}_l^d/i\omega\epsilon_b$. Finally, the objective function
231 of FFT-TSOM is

$$f_T(\bar{\beta}_l, \bar{\chi}) = \sum_{l=1}^{N_i} (F_D(\bar{\beta}_l) + F_S(\bar{\beta}_l, \bar{\chi})) \quad (11)$$

232 where $F_D(\bar{\beta}_l) = \Delta_l^{\text{fe}}(\bar{\beta}_l)/\|\bar{E}_l^{\text{sca}}\|^2$, and $F_S(\bar{\beta}_l, \bar{\chi}) = 232$
233 $\Delta_l^{\text{cur}}(\bar{\beta}_l, \bar{\chi})/\|\bar{E}_l^{\text{inc}}\|^2$. The optimization is to minimize
234 the objective function (11).

III. REGULARIZATION AND INVERSION ALGORITHM

235 Recently, to stabilize the solution of the inverse scattering
236 problem, van den Berg and Kleinmann (1995) incorporated
237 the total variation (TV) in an inverse scattering problem by
238 enhancing the modified gradient algorithm [35]. After that, the
239 multiplicative regularization technique is introduced in the MR-
240 CSI method based on the L_1 - and L_2 -norm TV as constraint
241 [20], [21]. In the MR-CSI method, the objective function is
242 composed of the original cost function, and the multiplicative
243 regularizer with a weighted L_2 -norm TV. The weighting param-
244 eter is determined and updated by the inversion result during the
245 optimization process.

247 However, the strategy of the regularization parameter used in
 248 the MR-CSI cannot be directly used in the FFT-TSOM. In the
 249 FFT-TSOM, only the most influential bases are utilized. Hence,
 250 the residues in the current equation and the filed equation in the
 251 FFT-TSOM could be much larger than the one in the CSI. In
 252 this paper, a novel adaptive regularization parameter updating
 253 strategy will be introduced.

254 First, with the inclusion of the multiplicative regularizer,
 255 the objective function, at the n th iteration of the optimization,
 256 becomes

$$\mathcal{H}_n(\bar{\beta}_l, \bar{\chi}) = f_T(\bar{\beta}_l, \bar{\chi}) \cdot F_n^{\text{MR}}(\chi) \quad (12)$$

257 where $\bar{\beta}_l$ and $\bar{\chi}$ are the unknowns, and the multiplicative
 258 regularizer is given as in [21]

$$F_n^{\text{MR}}(\chi) = \frac{1}{A} \int_D \frac{|\nabla \chi(\bar{r})|^2 + \delta_n^2}{|\nabla \chi_{n-1}(\bar{r})|^2 + \delta_n^2} d\bar{v}(\bar{r}) \quad (13)$$

259 where A is the area of the test domain D , and ∇ denotes the
 260 spatial differentiation with respect to \bar{r} . The constant regular-
 261 ization parameter δ_n^2 is introduced for restoring differentiability
 262 of the TV regularizer, and it plays a crucial role in the TV-
 263 type regularization. From [20], the effect of the regularization
 264 should be increased as a function of the number of the iterations
 265 by decreasing the regularization parameter δ_n^2 . Therefore, in
 266 the MR-CSI method, the regularization parameter is chosen as
 267 follows:

$$\delta_{\text{CSI}}^2 = \frac{F_S(\bar{\beta}_l, \bar{\chi})}{\Delta^2} \quad (14)$$

268 where Δ is the mesh size of the discretized domain D . Equation
 269 (14) is designed such that the value of δ_n^2 is decreased with
 270 the value of the objective function; thus, as the iterations
 271 proceed, the effect of multiplicative regularization is increased.
 272 In the beginning of optimization procedure, δ_n^2 is equal to δ_{CSI}^2 ,
 273 and when δ_{CSI}^2 almost keeps unchanged, then δ_n^2 is gradually
 274 reduced to a threshold by an exponential function, which can
 275 make sure that the problem remains convex [21]. The specific
 276 expression of δ_n^2 is given in the following algorithm sketch.

277 Following the names of two predecessors, the new inversion
 278 method is named as MR-FFT-TSOM, and it is implemented as
 279 follows:

280 Step 1) Calculate \bar{G}_S , \bar{G}_D , and the thin SVD of \bar{G}_S ; obtain
 281 \bar{I}_l^d from (6), $l = 1, 2, \dots, N_i$.

282 Step 2) Initialization, $n = 0$; $\bar{\chi}_0 = 0$; select M_F , and initial-
 283 ize $\bar{\beta}_{l,0} = 0$ according to the method in FFT-TSOM
 284 [31], $\bar{\rho}_{\beta;l,0}$ and $\bar{\rho}_{\varepsilon;0}$ are the search direction of $\bar{\beta}_l$ and
 285 $\bar{\chi}$, respectively. $\bar{\rho}_{\beta;l,0} = 0$ and $\bar{\rho}_{\varepsilon;0} = 0$.

286 Step 3) $n = n + 1$

287 Step 3.1) Update $\bar{\beta}_{l,n}$: $\bar{\beta}_{l,n} = \bar{\beta}_{l,n-1} + d_{\beta;l,n} \bar{\rho}_{\beta;l,n}$,
 288 where the scalar $d_{\beta;l,n}$ can be obtained
 289 according to $(\partial f_T / \partial d_{\beta;l,n}) = 0$. Calcu-
 290 late gradient (Frechet derivative) $\bar{g}_{\beta;l,n} =$
 291 $\nabla_{\bar{\beta}_l} f_T$ evaluated at $\bar{\beta}_{l,n-1}$ and $\bar{\chi}_{n-1}$; de-
 292 termine the CG search directions $\bar{\rho}_{\beta;l,n} =$
 293 $\bar{g}_{\beta;l,n} + (\text{Re}(\bar{g}_{\beta;l,n} - \bar{g}_{\beta;l,n-1}, \bar{g}_{\beta;l,n}) / \| \bar{g}_{\beta;l,n} \|)^2 \bar{\rho}_{\beta;l,n-1}$, $n \geq 1$ [6], [26].

295 Step 3.2) There are two step operations for updating 295
 296 the contrast, including before regulariza- 296
 297 tion and after regularization, respectively. 297
 298 Update the contrast before multiplicative 298
 299 regularization $\bar{\chi}_n^{\text{BMR}}$: for the m th subunit, 299
 300 $m = 1, 2, \dots, M$, utilizing $(\partial f_T / \partial \chi) = 0$, 300
 301 the solution is given by

$$\left(\bar{\chi}_n^{\text{BMR}} \right)_m = \frac{\sum_{l=1}^{N_i} \left(\bar{E}_{l,n}^{\text{tot}} \right)_m^* \cdot \left(\frac{\bar{I}_{l,n}}{-i\omega\varepsilon_b} \right)_m / \left\| \bar{E}_l^{\text{inc}} \right\|^2}{\sum_{l=1}^{N_i} \left(\bar{E}_{l,n}^{\text{tot}} \right)_m^* \cdot \left(\bar{E}_{l,n}^{\text{tot}} \right)_m / \left\| \bar{E}_l^{\text{inc}} \right\|^2} \quad (15)$$

302 where $(\bar{I}_{l,n})_m = (\bar{I}_{l,n}^d)_m + (\bar{I}_{l,n}^a)_m$ and 302
 303 the corresponding total electrical field in 303
 304 the m th subunit $(\bar{E}_{l,n}^{\text{tot}})_m = (\bar{E}_{l,n}^{\text{inc}})_m + 304$
 305 $(\bar{G}_D \cdot \bar{I}_{l,n})_m$. 305

306 Step 3.3) Update δ_n^2 : According to the obtained 306
 307 $\bar{\chi}_n^{\text{BMR}}$ and $\bar{\beta}_{l,n}$, calculate the $F_D(\bar{\beta}_{l,n})$ 307
 308 and $F_S(\bar{\beta}_{l,n}, \bar{\chi}_n^{\text{BMR}})$. When $n > 5$, if six 308
 309 consecutive values of $\delta_{\text{CSI}}^2 = F_S(\bar{\beta}_{l,n}, 309$
 $\bar{\chi}_n^{\text{BMR}}) / \Delta^2$ nearly keep unchanged, then 310
 $\delta_n^2 = \delta_{\text{CSI}}^2 \times e^{-(\alpha(M_u/2-M_F)(n-N_\kappa)/N_\kappa)}$, 311
 312 where M_F is the size of blocks in the 312
 313 four corners of the coefficient tensor [31], 313
 314 and N_κ is the iteration number when the 314
 315 average of the previous five consecutive 315
 316 variance of δ_{CSI}^2 is less than a small con- 316
 317 stant value κ ($\kappa = \delta_{\text{CSI}}^2 / 10$), M_u is simply 317
 318 chosen as the smaller number of of M_x 318
 319 and M_y , which are the total number of 319
 320 cells along the x - and y -directions, repe- 320
 321 tively, and we assume that $M_x \leq M_y$ here, 321
 322 regardless if the domain is rectangular 322
 323 or square, and the value of $\alpha > 0$ will be 323
 324 discussed in the numerical simulation 324
 325 part. The reason we choose such a 325
 326 parameter is that, as the optimization 326
 327 proceeds, the regularization effect will 327
 328 become strong even when using the FFT- 328
 329 TSOM model ing. Otherwise, $\delta_n^2 = \delta_{\text{CSI}}^2$. 329
 330 On the other hand, as mentioned 330
 331 in [21], to keep convexity for real 331
 $d_{\varepsilon,n}$, δ_n^2 should be larger than the value 332
 $(1/2)(\|\nabla \chi_n / \sqrt{A(|\nabla \chi_n|^2 + \delta_{n-1}^2)}\|_D^2 / \|1 / 333$
 $\sqrt{A(|\nabla \chi_n|^2 + \delta_{n-1}^2)}\|_D^2)$. 334

335 Step 3.4) Update $\bar{\chi}_n^{\text{MR}}$ (the contrast after multi- 335
 336 plicative regularization): The regularized 336
 337 updated contrast $(\bar{\chi}_n^{\text{MR}})_m = (\bar{\chi}_n^{\text{BMR}})_m + 337$
 $(d_{\varepsilon,n} \bar{\rho}_{\varepsilon,n})_m$ where $\bar{\rho}_{\varepsilon,n}$ is the conjugate 338
 339 gradient direction $\bar{\rho}_{\varepsilon,n} = \bar{g}_{\varepsilon,n} + (\text{Re} \times 339$
 $\langle \bar{g}_{\varepsilon,n} - \bar{g}_{\varepsilon,n-1}, \bar{g}_{\varepsilon,n} \rangle / \bar{g}_{\varepsilon,n} \bar{\rho}_{\varepsilon,n-1}, n \geq 1)$, 340
 $\bar{g}_{\varepsilon,n} = (\nabla_{\chi} \mathcal{H}_n(\bar{\beta}_l, \bar{\chi}) / \sum_{l=1}^{N_i} \|\bar{E}_{l,n}^{\text{tot}}\|^2)$ eval- 341
 342 uated at $\bar{\chi}_n^{\text{BMR}}$ with the previous mini- 342
 343 mization before regularization when the 343

gradient of $F_S(\bar{\beta}_{l,n}, \bar{\chi})$ with respect to the changes in the contrast around the point $\bar{\chi} = \bar{\chi}_n^{\text{BMR}}$ vanishes. Thus, $\bar{g}_{\varepsilon,n} = (F_D(\bar{\beta}_{l,n}) + F_S(\bar{\beta}_{l,n}, \bar{\chi}))((\partial F_n^{\text{MR}}(\chi)/\partial \chi)_\chi = \chi_n^{\text{BMR}} / \sum_{l=1}^{N_i} \|\bar{E}_{l,n}^{\text{tot}}\|^2)$ being a preconditioned gradient of the regularization factor $F_n^{\text{MR}}(\chi)$ with respect to the changes in the contrast around the point $\chi = \chi_n^{\text{BMR}}$. In addition, the real parameter $d_{\varepsilon,n}$ can be found from a line minimization as done in [20].

Step 4) if the termination condition is satisfied, stop optimization. Otherwise, go to step 3. Empirically, we stop the optimization when the values of the contrast do not noticeably change for successive five iterations.

We mention in passing that when the MR is applied to SOM, the optimization procedure can be considered as a special case of the aforementioned procedure where all the Fourier bases in MR-FFT-TSOM are used, i.e., the MR-SOM can be considered as a special case of MR-FFT-TSOM.

IV. NUMERICAL EXPERIMENT AND DISCUSSION

Here, to test the proposed MR-FFT-TSOM, we present several numerical examples in the 2-D TM case. In all tests in this section, additive white Gaussian noise (AWGN) is added to the numerical scattering results and is quantified by $(\|\bar{e}_l\|/\|\bar{e}_l\|/\|\bar{E}_{l,\text{MOM}}^{\text{sca}}\|/\|\bar{E}_{l,\text{MOM}}^{\text{sca}}\|) \times 100\%$, where $\bar{E}_{l,\text{MOM}}^{\text{sca}}$ is the numerical scattering results for the l th incidence, so that $\bar{E}_l^{\text{sca}} = \bar{E}_{l,\text{MOM}}^{\text{sca}} + \bar{e}_l$. The $\bar{E}_{l,\text{MOM}}^{\text{sca}}$ are generated by MoM using finer grid meshes than the ones used in the inversions.

In the following tests, the DoI is a $2 \text{ m} \times 2 \text{ m}$ square centered at the origin. The scatterers are illuminated by 16 incidences at 400 MHz (the corresponding wavelength $\lambda = 0.75 \text{ m}$) incident from different angles evenly distributed in $[0, 2\pi]$ on a circle with 3-m radius centered at the origin. The scattered fields are collected by an antenna array with 32 antennas uniformly distributed along the same circle with 3-m radius. In all the simulations, a 64×64 grid mesh of the DoI is used for our reconstructions. As for the scattered fields in the forward-scattering problem, they are calculated by the MoM method with a 100×100 grid mesh. We choose the $L = 15$ throughout through all the simulations as in [26].

In the first case, we considered the profile mentioned in [31], which consists of two discs, a coated rectangle, and the background material, as shown in Fig. 1. The two disks are centered at $(-0.4, 0.6) \text{ m}$ and $(0.4, 0.6) \text{ m}$ with the same 0.3-m radius and the same relative permittivity $\varepsilon_r = 2.3$, $\varepsilon_r = \varepsilon/\varepsilon_b$. The coated rectangle is centered at $(0, -0.3) \text{ m}$. The inner rectangle has a 1-m-long edge and a 0.6-m-short range, whereas the outer rectangle has a 1.6-m-long edge and a 1-m-short edge. The relative permittivity of the inner rectangle is $\varepsilon_r = 2 + i0.5$, whereas the outer one is $\varepsilon_r = 1.5 + i0.2$.

As we know in [31], the SOM cannot obtain a basic and satisfactory reconstruction result of the given profile. As depicted in Fig. 3, when the noise level is 10% AWGN, if we

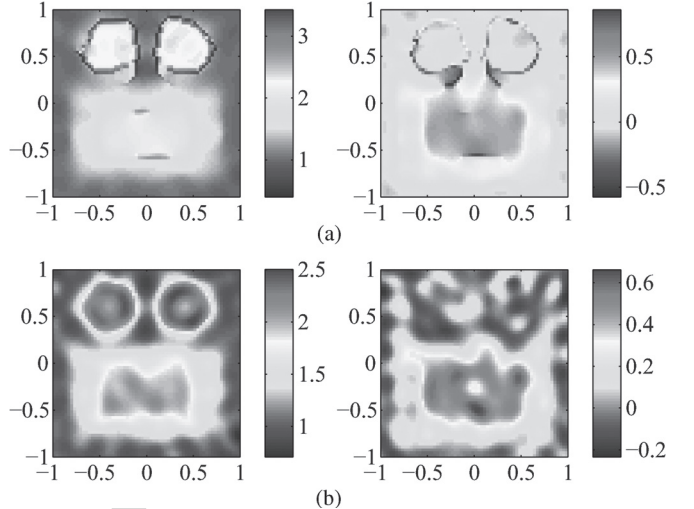


Fig. 3. Reconstruction results by MR-SOM with 10% AWGN, the (left) real and (right) imaginary part of the reconstruction relative permittivity ε_r when (a) $\delta_n^2 = \delta_{\text{CSI}}^2$ and (b) $\delta_n^2 = \delta_{\text{CSI}}^2 \times 2^3$ after 1000 iterations.

use the $\delta_{\text{CSI}}^2 = F_S(\bar{\beta}_l, \bar{\chi})/\Delta^2$ directly from the paper of van den Berg [21], the results in Fig. 3(a) show that MR works in the MR-SOM but cannot attain the expected effect compared with the exact profile. However, if the regularization parameter is modified to $\delta_n^2 = \delta_{\text{CSI}}^2 \times 2^3$, a significant change can be observed in Fig. 3(b), where the permittivity of the profile is more accurate, and a better effect on edge preserving can be observed compared with Fig. 3(a). Under the 30% AWGN, the reconstruction results are shown in Fig. 4, the result after 1000 iterations in Fig. 4(a) utilizing the regularization parameter δ_{CSI}^2 is significantly better than $\delta_n^2 = \delta_{\text{CSI}}^2 \times 2^3$ after 1500 iterations in Fig. 4(b), in which the reconstruction result almost cannot be recognized. This is probably due to the reason that, when the noise level is higher, the residue of the current equation is larger, i.e., $F_S(\bar{\beta}_l, \bar{\chi})$, and the regularization parameter δ_n^2 is also larger so that the MR almost does not work in the MR-SOM. Fig. 4(a) shows that once δ_n^2 is gradually reduced to a smaller value, which is close to the threshold in [21], a better reconstructed result can be obtained. Consequently, from these results, the MR can work in the MR-SOM and achieve a better performance than the SOM only can obtain. The above numerical results provide strong evidence that the effect of the MR-SOM largely depends on the selection of the regularization parameter δ_n^2 , and it is greatly influenced by the level of noise. This fact requires that a suitable principle for the regularization should be given to make the algorithm more robust and stable, which is, however, not an easy task. In Section III, a new regularization principle is proposed in MR-FFT-TSOM. In fact, when all the Fourier bases in MR-FFT-TSOM are used, MR-FFT-TSOM is equivalent to MR-SOM. The following numerical results will show that MR-FFT-TSOM with the new regularization principle produces a quite stable result and is much less influenced by noise.

In the following, the performance of the MR-FFT-TSOM is examined using the same profile as above. Here, we choose $\alpha = 2/25$, which means that when $M_F = 7$, $\alpha(M_x/2 - M_F) = 2$. The reason to do so is just to choose a properly decreasing parameter δ_n^2 as optimization proceeds. Using the same synthetic data in MR-SOM, numerical results to evaluate the

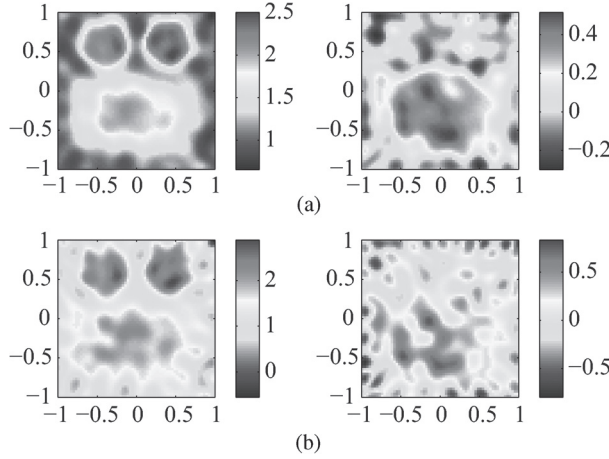


Fig. 4. Reconstruction results by MR-SOM with 30% AWGN, the (left) real and (right) imaginary part of the reconstruction relative permittivity ε_r when (a) $\delta_n^2 = \delta_{CSI}^2$ after 1000 iterations and (b) $\delta_n^2 = \delta_{CSI}^2 \times 2^3$ after 1500 iterations.

437 performance of the proposed MR-FFT-TSOM are presented.
438 First, 10% AWGN is added to the synthetic data. First, $M_F = 7$
439 and $M_F = 12$ are chosen for the reconstruction with the initial
440 guess being background. After one round of optimization with
441 750 iterations, the final reconstructed results for $M_F = 7$ and
442 $M_F = 12$ are shown in Figs. 5(a) and 6(a), respectively. We
443 see that the reconstructed results by MR-FFT-TSOM are much
444 better than that of MR-SOM. Moreover, compared with the
445 initial profile in Fig. 2, the imaginary part of the permittiv-
446 ity reconstructed with $M_F = 7$ is more accurate than $M_F =$
447 12, observed from the value in Figs. 5 and 6. However, the
448 profile reconstructed by $M_F = 12$ is more shaped-preserved
449 and differentiable than the one using $M_F = 7$, particularly
450 for the real part. These two figures further prove that small
451 values of M_F have higher capabilities for noise suppression;
452 nonetheless, large values of M_F show increased resolution for
453 the image reconstruction. The reason is that more high-order
454 components of the current subspace are considered so that we
455 can reconstruct an image with high resolution. Therefore, the
456 M_F balances the robustness against noise and the resolution
457 of the reconstruction. Moreover, when $\delta_n^2 = \delta_{CSI}^2$, the recon-
458 structed results when $M_F = 7$ and $M_F = 12$ can be obtained in
459 Figs. 5(b) and 6(b), respectively. Figs. 5(c) and 6(d) show δ_n^2 for
460 $M_F = 7$ and $M_F = 12$, respectively. The figures inside show
461 how δ_n^2 change after switching to the exponentially tunable
462 regularization and the corresponding $N_\kappa = 244, 220$. After the
463 changing point, the ratio between δ_{CSI}^2 and δ_n^2 is not large, i.e.,
464 about 4 on average. We see that when the noise level is 10%
465 AWGN, using $\delta_n^2 = \delta_{CSI}^2$ or δ_n^2 proposed in this paper, almost
466 the same reconstructed results can be obtained in MR-FFT-
467 TSOM. This is due to the fact that both principles are far less
468 than the produced $|\nabla\chi(\bar{r})|^2$, which means that when the noise
469 level is not high, the δ_{CSI}^2 is already enough. However, in the
470 following example, we will see that when the noise level is high,
471 there will be a difference between the two principles.
472 Before testing with the highly noisy data, we examine the
473 robustness of the proposed MR-FFT-TSOM compared with the
474 original FFT-TSOM. Fig. 6(c) shows the reconstruction result
475 obtained by successive multiple rounds of optimization by MR-
476 FFT-TSOM using $M_F = 5, M_F = 6$, and $M_F = 12$, with 300,

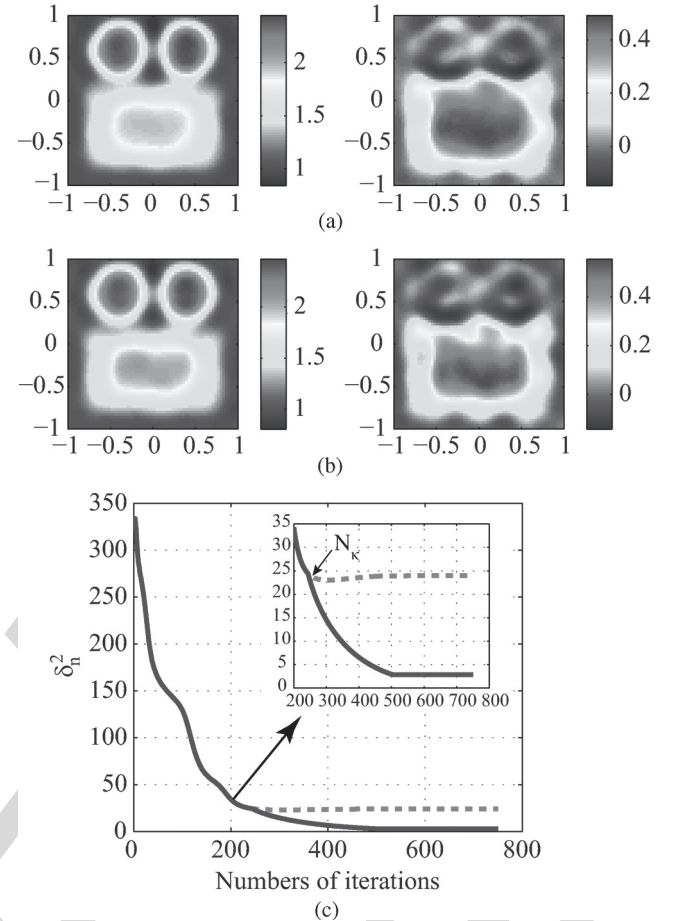


Fig. 5. Reconstruction results by MR-FFT-TSOM with 10% AWGN, the (left) real and (right) imaginary part of the reconstruction relative permittivity ε_r by (a) $M_F = 7$ after 750 iterations when $\delta_n^2 = \delta_{CSI}^2 \times e^{-(2/25)(32-M_F)(n-N_\kappa)/N_\kappa}$ and (b) $M_F = 7$ after 750 iterations when $\delta_n^2 = \delta_{CSI}^2$. (c) δ_n^2 versus the iterations, $\delta_n^2 = \delta_{CSI}^2$ (dotted red line) and $\delta_n^2 = \delta_{CSI}^2 \times e^{-(2/25)(32-M_F)(n-N_\kappa)/N_\kappa}$ (blue line). The figure inside illustrates the comparison from the switching point $N_\kappa = 244$.

300, and 150 iterations, respectively. The optimization results, 477 i.e., $\bar{\beta}_l$ and $\bar{\chi}$, obtained for the last iteration of the previous 478 round are set as the initial values to of the next round of opti- 479 mization. Here, we see that there is no improvement between 480 Fig. 6(a) and (c). Unlike FFT-TSOM [31], MR-FFT-TSOM 481 does not need to execute several rounds of optimization using 482 different numbers of the current subspace basis successively. 483 Furthermore, the proposed MR-FFT-TSOM has superior stabil- 484 ity and robustness compared with TSOM-based reconstruction 485 algorithms. 486

Second, we further investigate the performance of the MR- 487 FFT-TSOM with 30% AWGN added to the synthetic data. The 488 reconstruction results after 750 iterations by one round of opti- 489 mization under $M_F = 7$ and $M_F = 12$ are depicted in Fig. 7(a) 490 and (b), respectively. When the noise level is high, we see 491 that the reconstruct permittivity by $M_F = 7$ is more accurate 492 than by $M_F = 12$. Although the reconstructed profiles are a bit 493 distorted in Fig. 7, the results reconstructed by MR-FFT-TSOM 494 are better than that reconstructed by FFT-TSOM [31]. Because 495 MR-FFT-TSOM has twofold ability of the noise suppression, 496 not only TSOM but also the multiplicative regularization can 497 filter out the noise in the optimization procedure. When the 498

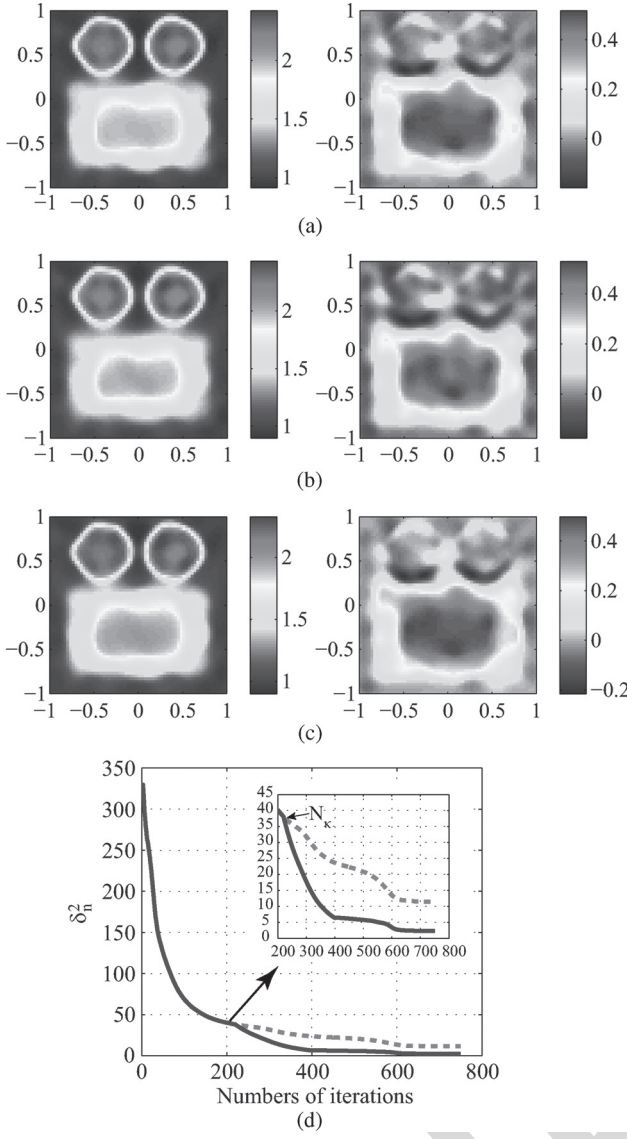


Fig. 6. Reconstruction results by MR-FFT-TSOM with 10% AWGN, the (left) real and (right) imaginary part of the reconstruction relative permittivity ε_r when (a) $M_F = 12$ and $\delta_n^2 = \delta_{CSI}^2 \times e^{-(2/25)(32-M_F)(n-N_\kappa)/N_\kappa}$ after 750 iterations and (b) $M_F = 12$ and $\delta_n^2 = \delta_{CSI}^2$ after 750 iterations. (c) Using three successive rounds of optimization, $M_F = 5$, $M_F = 6$, and $M_F = 12$ with 300, 300, and 150 iterations, respectively, when $\delta_n^2 = \delta_{CSI}^2 \times e^{-(2/25)(32-M_F)(n-N_\kappa)/N_\kappa}$. (d) δ_n^2 versus the iterations $M_F = 12$, $\delta_n^2 = \delta_{CSI}^2$ (dotted red line) and $\delta_n^2 = \delta_{CSI}^2 \times e^{-(2/25)(32-M_F)(n-N_\kappa)/N_\kappa}$ (blue line). The figure inside illustrates the comparison from the switching point $N_\kappa = 220$.

499 noise level is high, the residue of the field equation and the 500 gradient of the contrast will be large, and then, the noise will be 501 suppressed in the optimization procedure as mentioned in [21]. 502 Moreover, we also get the reconstructed results using $\delta_n^2 = \delta_{CSI}^2$ 503 under $M_F = 7$ and $M_F = 12$. When using $M_F = 7$, the two 504 principles show almost the same performance (the proposed 505 principle might give a slightly better result if one carefully 506 looks into the imaginary part of the reconstructed profile), as 507 shown in Fig. 7(a) and (c). This is mainly due to the strong 508 regularization effect of using a low dimension of the current 509 subspace. However, when using $M_F = 12$, which means that 510 the current subspace being used is no longer that low, one sees 511 that the result obtained with proposed principle, as depicted

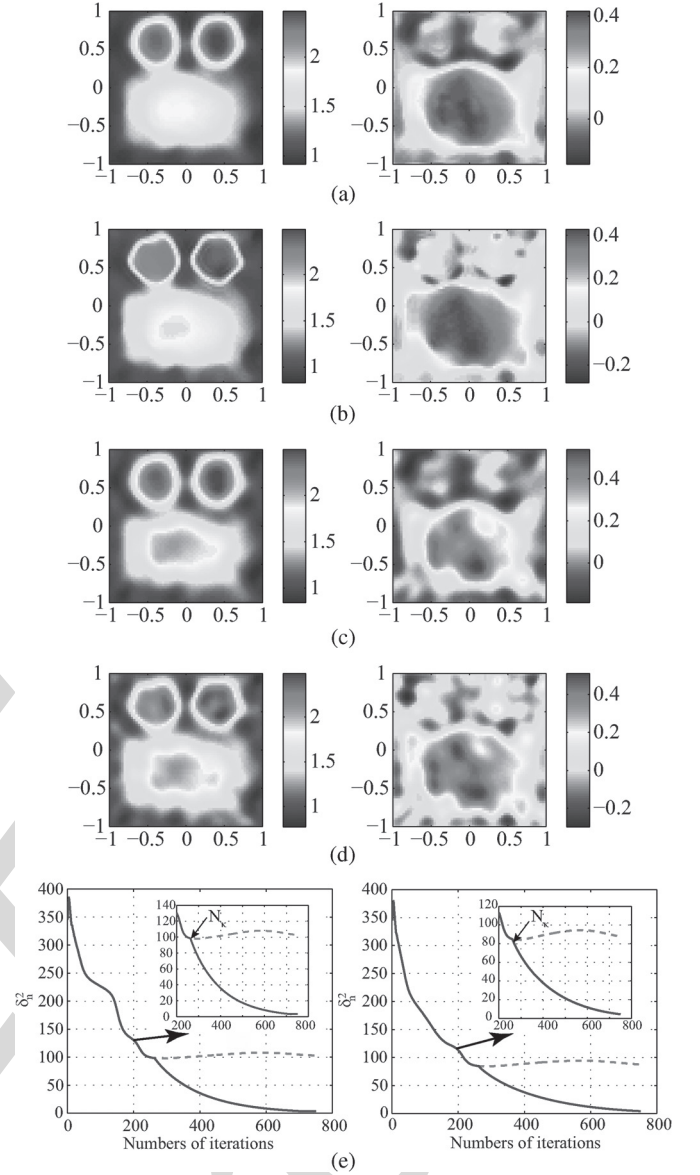


Fig. 7. Reconstruction results by MR-FFT-TSOM with 30% AWGN, the (left) real and (right) imaginary part of the reconstruction relative permittivity ε_r when (a) $M_F = 7$ and $\delta_n^2 = \delta_{CSI}^2 \times e^{-(2/25)(32-M_F)(n-N_\kappa)/N_\kappa}$ after 750 iterations; (b) $M_F = 12$ and $\delta_n^2 = \delta_{CSI}^2 \times e^{-(2/25)(32-M_F)(n-N_\kappa)/N_\kappa}$ after 750 iterations; (c) $M_F = 7$ and $\delta_n^2 = \delta_{CSI}^2$ after 750 iterations; (d) $M_F = 12$ and $\delta_n^2 = \delta_{CSI}^2$ after 750 iterations; (e) δ_n^2 versus the iterations, $\delta_n^2 = \delta_{CSI}^2$ (dotted red line) and $\delta_n^2 = \delta_{CSI}^2 \times e^{-(2/25)(32-M_F)(n-N_\kappa)/N_\kappa}$ (blue line), $M_F = 7$ (left) and $M_F = 12$ (right). The figures inside illustrate the comparison from the switching points $N_\kappa = 263, 261$, respectively.

in Fig. 7(b), is obviously better than the one with the CSI 513 principle, as depicted in Fig. 7(d). As shown in Fig. 7(e), the 513 numbers of switching points between δ_n^2 and δ_{CSI}^2 for $M_F = 514$ 7 and $M_F = 12$ are $N_\kappa = 263, 261$, respectively. After the 515 switching point, the ratio between δ_n^2 and δ_{CSI}^2 is large, i.e., 516 about 10 on average. This is due to the fact that the proposed 517 principle brings a stronger MR effect compared with the CSI 518 principle. Since one can obtain more information of the induced 519 current as well as the reconstructed profile when using a higher 520 dimension of the current subspace, the proposed principle is the 521 preferred principle being used in MR-FFT-TSOM. Therefore, 522

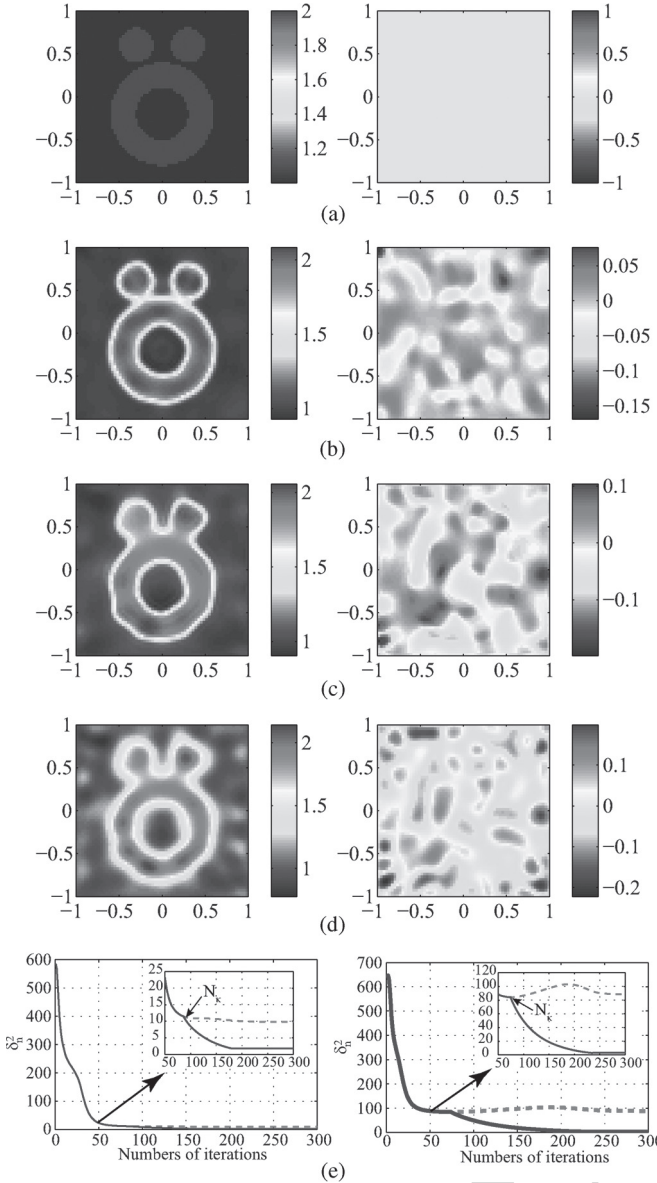


Fig. 8. (a) Exact Austria profile of DoI. Reconstruction result by the MR-FFT-TSOM after 300 iterations (b) when $M_F = 12$ and $\delta_n^2 = \delta_{\text{CSI}}^2 \times e^{-((2/25)(32-M_F)(n-N_\kappa)/N_\kappa)}$ with 10% AWGN; (c) when $M_F = 12$ and $\delta_n^2 = \delta_{\text{CSI}}^2 \times e^{-((2/25)(32-M_F)(n-N_\kappa)/N_\kappa)}$ with 30% AWGN; (d) when $M_F = 12$ and $\delta_n^2 = \delta_{\text{CSI}}^2$ with 30% AWGN; (e) δ_n^2 versus the iterations, $\delta_n^2 = \delta_{\text{CSI}}^2$ (dotted red line) and $\delta_n^2 = \delta_{\text{CSI}}^2 \times e^{-((2/25)(32-M_F)(n-N_\kappa)/N_\kappa)}$ (blue line), 10% AWGN (left) and 30% AWGN (right). The figures inside illustrate the comparison from the switching points $N_\kappa = 86, 74$, respectively.

we see that the proposed MR-FFT-TSOM not only inherits the merits of the FFT-TSOM but also holds the property of edge preserving in image restoration. Moreover, it is more stable and has better robustness against noise compared with FFT-TSOM. Above are the comparisons among MR-FFT-TSOM, MR-SOM, and FFT-TSOM by the inversion of the profile proposed in [31]. In the second case, we will further examine the effect of the proposed MR-FFT-TSOM by a classical and well-known Austria profile, which consists of an annular, two disks, and the background material [26]. The two disks are of the same 0.2-m radius, and their centers are $(-0.3, 0.6)$ m and $(0.3, 0.6)$ m. The annual is centered at $(0, -0.2)$ m with 0.3-m

inner radius and 0.6-m outer radius. All three scatters have the same relative permittivity $\varepsilon_r = 2$, as shown in Fig. 8(a). In this case, as previously mentioned, to keep the property of edge preserving, $M_F = 12$ is considered as the best choice for the Austria profile. The retrieval result after 300 iterations with 10% AWGN was shown in Fig. 8(b). We see that MR-FFT-TSOM gave a quite satisfactory result, which was quite close to the exact profile both in the shape of the profile or the accuracy of the permittivity. Further, we carried on the test to investigate the noise suppressions ability of the MR technique when the synthetic data are corrupted by 30% random additive white noise. In Fig. 8(c), we see that a satisfying reconstruction image after 300 iterations still can be obtained. As before, we also examine the performance of the MR-FFT-TSOM using $\delta_n^2 = \delta_{\text{CSI}}^2$ under 30% AWGN, which is shown in Fig. 8(d), where we see that the effect of edge preserving in MR is not such obvious. The numbers of switching points between δ_n^2 and δ_{CSI}^2 for 10% and 30% AWGN are $N_\kappa = 86, 74$, respectively, as shown in Fig. 8(e). Hence, the stability and effectiveness of the strategy of the regularization parameter δ_n^2 in the proposed MR-FFT-TSOM is further verified by various cases.

To further validate the proposed algorithm, MR-FFT-TSOM and FFT-TSOM were tested on the 2005 Fresnel data set [36]. Here, we present results from the *FoamTwinDiel* data set, which was collected for 18 transmitters, 241 receivers, and 9 frequencies from 2 to 10 GHz. The scatters, which consist of two smaller cylinders of relative permittivity $\varepsilon_r = 2$ with diameter = 3.1 cm where one of the smaller cylinders is embedded in a larger cylinder with $\varepsilon_r = 1.45$, diameter = 8 cm, are shown in Fig. 9(a). In the experimental case, a 45×45 grid mesh of the DoI, which is 15 cm \times 15 cm square centered at the origin, is used for the reconstruction. To calibrate the data, we make use of the method as outlined [36]. It is worth mentioning that all the numerical reconstructions are proceeded at a single frequency of 4 GHz instead of frequency hopping. According to the property of SVD of \bar{G}_S , $L = 10$ and $M_F = 12$ is considered as the choice for all the numerical simulation. The reconstructed results by the proposed MR-FFT-TSOM after 750 iterations are shown in Fig. 9(b). It is seen that the retrieval result exhibits an excellent effect of edge preserving and is quite satisfying. Similarly, the retrieval results after 750 iterations by FFT-TSOM and MR-FFT-TSOM when $\delta_n^2 = \delta_{\text{CSI}}^2$ are shown in Fig. 9(c) and (d), respectively. Fig. 9(e) shows δ_n^2 -iteration plot. The number of switching points between δ_n^2 and δ_{CSI}^2 is $N_\kappa = 86$. After the switching point, the ratio between δ_n^2 and δ_{CSI}^2 is more than 10. Although the results reconstructed by FFT-TSOM also can be a satisfying image, there is still not small disparity compared with the proposed MR-FFT-TSOM. Moreover, we can see that, only depending on data at a single frequency, MR-FFT-TSOM with $\delta_n^2 = \delta_{\text{CSI}}^2$ nearly could not reconstruct the satisfied image. However, as outlined in [37], significantly better results can be obtained with frequency-hopping inversion. Therefore, the proposed MR-FFT-TSOM exhibits excellent performance by both synthetic data and experimental data set. These figures reveal that the proposed MR-FFT-TSOM exhibit a better and more satisfying reconstruction effect compared with the results in SOM [26], TSOM [29], FFT-TSOM [31], and MR-SOM as well.

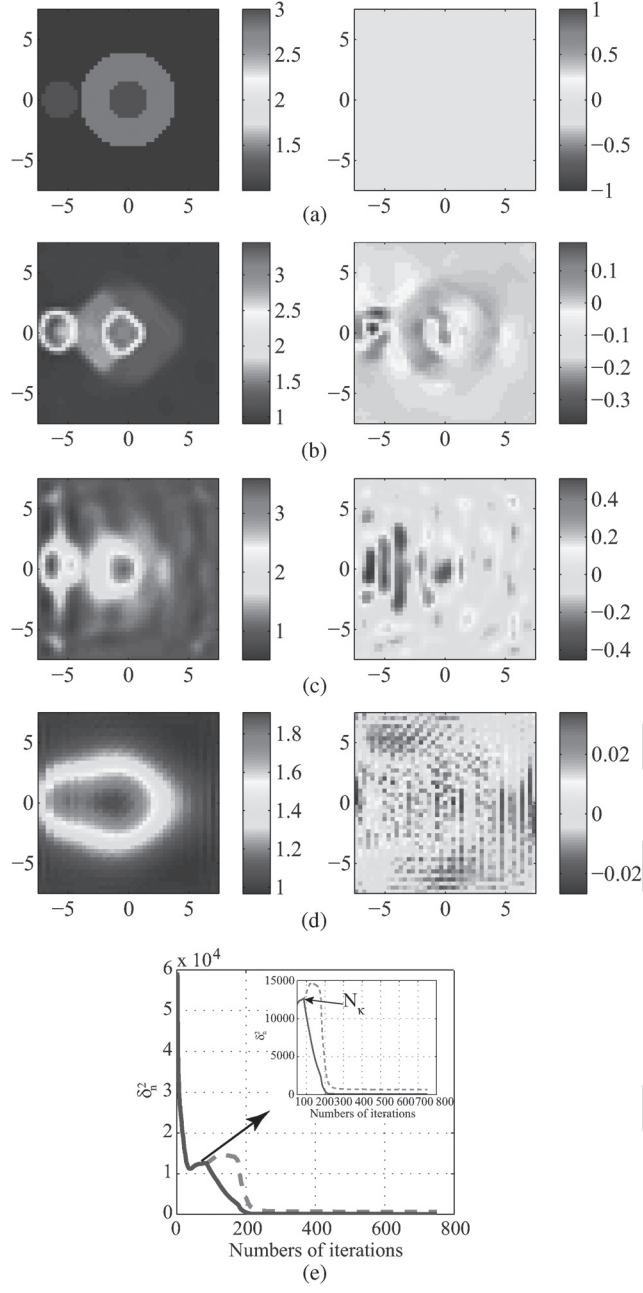


Fig. 9. Reconstruction of Fresnel data set *FoamTwinDiel*. (a) Exact profile of DOI. (b) Reconstruction result by the MR-FFT-TSOM using the proposed regularization parameter. (c) Reconstruction result by the FFT-TSOM. (d) Reconstruction result by the MR-FFT-TSOM when $\delta_n^2 = \delta_{\text{CSI}}^2$. (e) δ_n^2 versus the iterations, $\delta_n^2 = \delta_{\text{CSI}}^2$ (dotted red line) and $\delta_n^2 = \delta_{\text{CSI}}^2 \times e^{-((2/25)(32-M_F)(n-N_\kappa)/N_\kappa)}$ (blue line). The figure inside illustrates the comparison from the switching point $N_\kappa = 86$.

593

V. CONCLUSION

In this paper, we have proposed a new MR-FFT-TSOM for solving inverse scattering problems. In FFT-TSOM, the current subspace is spanned by discrete Fourier bases, and only the most influential bases are used. Based on the rule of the regularization parameter in MR-CSI, a modified and more stable and effective principle of the regularization parameter is put forward according to the property of the FFT-TSOM. The proposed MR-FFT-TSOM inherits the advantages of the FFT-TSOM earlier in [31], i.e., lower computational complexity

than the TSOM, better stability of the inversion procedure, and better robustness against noise compared with the SOM. Moreover, owing to the effect of the MR, the proposed MR-FFT-TSOM has twofold ability of noise suppression and the property of edge preserving, which outperform the FFT-TSOM. As can be seen from the numerical inversion results on both the synthetic data and experimental data shown in this paper and those in [26], [29], and [31], the performance of the MR-FFT-TSOM is superior to SOM, MR-SOM, TSOM, and FFT-TSOM. Although our experiments are set up for the 2-D TM case, it should be pointed out that the MR-FFT-TSOM can be readily extended to 2-D TE and 3-D cases as well.

REFERENCES

- [1] Y. Wang and W. Chew, "An iterative solution of the two-dimensional electromagnetic inverse scattering problem," *Int. J. Imag. Syst. Technol.*, vol. 1, no. 1, pp. 100–108, 1989.
- [2] W. Chew and Y. Wang, "Reconstruction of two-dimensional permittivity distribution using the distorted Born iterative method," *IEEE Trans. Med. Imag.*, vol. 9, no. 2, pp. 218–225, Jun. 1990.
- [3] Q. H. Liu *et al.*, "Active microwave imaging. I. 2-D forward and inverse scattering methods," *IEEE Trans. Microw. Theory Tech.*, vol. 50, no. 1, pp. 123–133, Jan. 2002.
- [4] L.-P. Song, C. Yu, and Q. H. Liu, "Through-Wall Imaging (TWI) by radar: 2-D tomographic results and analyses," *IEEE Trans. Geosci. Remote Sens.*, vol. 43, no. 12, pp. 2793–2798, Dec. 2005.
- [5] P. M. Van Den Berg and R. E. Kleinman, "A contrast source inversion method," *Inverse Problems*, vol. 13, no. 6, pp. 1607–1620, Dec. 1997.
- [6] P. M. van den Berg, A. Van Broekhoven, and A. Abubakar, "Extended contrast source inversion," *Inverse Problems*, vol. 15, no. 5, pp. 1325–1344, Oct. 1999.
- [7] P. Mojabi and J. LoVetri, "Overview and classification of some regularization techniques for the Gauss–Newton inversion method applied to inverse scattering problems," *IEEE Trans. Antennas Propag.*, vol. 57, no. 9, pp. 2658–2665, Sep. 2009.
- [8] P. Mojabi and J. LoVetri, "Microwave biomedical imaging using the multiplicative regularized Gauss–Newton inversion," *IEEE Antennas Wireless Propag. Lett.*, vol. 8, pp. 645–648, 2009.
- [9] P. Mojabi and J. LoVetri, "Comparison of TE and TM inversions in the framework of the Gauss–Newton method," *IEEE Trans. Antennas Propag.*, vol. 58, no. 4, pp. 1336–1348, Apr. 2010.
- [10] J. Li, H. Liu, and J. Zou, "Multilevel linear sampling method for inverse scattering problems," *SIAM J. Sci. Comput.*, vol. 30, no. 3, pp. 1228–1250, 2008.
- [11] M. Pastorino, "Stochastic optimization methods applied to microwave imaging: A review," *IEEE Trans. Antennas Propag.*, vol. 55, no. 3, pp. 538–548, Mar. 2007.
- [12] P. Rocca, M. Benedetti, M. Donelli, D. Franceschini, and A. Massa, "Evolutionary optimization as applied to inverse scattering problems," *Inverse Problems*, vol. 25, no. 12, pp. 123 003-1–123 003-41, Dec. 2009.
- [13] C.-H. Huang, C.-C. Chiu, C.-L. Li, and K.-C. Chen, "Time domain inverse scattering of a two-dimensional homogenous dielectric object with arbitrary shape by particle swarm optimization," *Progr. Electromagn. Res.*, vol. 82, pp. 381–400, 2008.
- [14] T. Isernia, L. Crocco, and M. D'Urso, "New tools and series for forward and inverse scattering problems in lossy media," *IEEE Geosci. Remote Sens. Lett.*, vol. 1, no. 4, pp. 327–331, Oct. 2004.
- [15] L. Crocco, M. D'Urso, and T. Isernia, "Testing the contrast source extended Born inversion method against real data: The TM case," *Inverse Problems*, vol. 21, no. 6, pp. S33–S50, Dec. 2005.
- [16] I. Catapano, L. Crocco, M. D'Urso, and T. Isernia, "A novel effective model for solving 3-D nonlinear inverse scattering problems in lossy scenarios," *IEEE Geosci. Remote Sens. Lett.*, vol. 3, no. 3, pp. 302–306, Jul. 2006.
- [17] I. Catapano, L. Crocco, M. D'Urso, and T. Isernia, "3D microwave imaging via preliminary support reconstruction: Testing on the Fresnel 2008 database," *Inverse Problems*, vol. 25, no. 2, pp. 024002-1–024002-23, Feb. 2009.
- [18] M. D'Urso, T. Isernia, and A. F. Morabito, "On the solution of 2-D inverse scattering problems via source-type integral equations," *IEEE Trans. Geosci. Remote Sens.*, vol. 48, no. 3, pp. 1186–1198, Mar. 2010.

- 673 [19] A. Abubakar, P. M. Van den Berg, and J. J. Mallorqui, "Imaging of
674 biomedical data using a multiplicative regularized contrast source inver-
675 sion method," *IEEE Trans. Microw. Theory Tech.*, vol. 50, no. 7, pp. 1761–
676 1771, Jul. 2002.
677 [20] P. Abubakar, "Contrast source inversion method: State of art," *Prog.
678 Electromagn. Res.*, vol. 34, pp. 189–218, 2001.
679 [21] P. M. van den Berg, A. Abubakar, and J. T. Fokkema, "Multiplicative
680 regularization for contrast profile inversion," *Radio Sci.*, vol. 38, no. 2,
681 pp. 231–23–10, Apr. 2003.
682 [22] A. Abubaker and P. M. Van Den Berg, "Total variation as a multiplicative
683 constraint for solving inverse problems," *IEEE Trans. Image Process.*,
684 vol. 10, no. 9, pp. 1384–1392, Sep. 2001.
685 [23] A. Abubakar, P. M. Van Den Berg, T. M. Habashy, and H. Braunsch,
686 "A multiplicative regularization approach for deblurring problems," *IEEE
687 Trans. Image Process.*, vol. 13, no. 11, pp. 1524–1532, Nov. 2004.
688 [24] X. Chen, "Application of signal-subspace and optimization methods in
689 reconstructing extended scatterers," *J. Opt. Soc. Amer. A*, vol. 26, no. 4,
690 pp. 1022–1026, Apr. 2009.
691 [25] X. Ye, Y. Zhong, and X. Chen, "Reconstructing perfectly electric con-
692 ductors by the subspace-based optimization method with continuous
693 variables," *Inverse Problems*, vol. 27, no. 5, pp. 055011–1–055011–14,
694 May 2011.
695 [26] X. Chen, "Subspace-based optimization method for solving inverse-
696 scattering problems," *IEEE Trans. Geosci. Remote Sens.*, vol. 48, no. 1,
697 pp. 42–49, Jan. 2010.
698 [27] Y. Zhong, X. Chen, and K. Agarwal, "An improved subspace-based op-
699 timization method and its implementation in solving three-dimensional
700 inverse problems," *IEEE Trans. Geosci. Remote Sens.*, vol. 48, no. 10,
701 pp. 3763–3768, Oct. 2010.
702 [28] X. Ye, X. Chen, Y. Zhong, and R. Song, "Simultaneous reconstruction of
703 dielectric and perfectly conducting scatterers via T-matrix method," *IEEE
704 Trans. Antennas Propag.*, vol. 61, no. 7, pp. 3774–3781, Jul. 2013.
705 [29] Y. Zhong and X. Chen, "Twofold subspace-based optimization method
706 for solving inverse scattering problems," *Inverse Problems*, vol. 25, no. 8,
707 pp. 085003–1–085003–11, Aug. 2009.
708 [30] Y. Zhong, "Subspace-based inversion methods for solving electromagnetic
709 inverse scattering problems," Ph.D. dissertation, Nat. Univ. Singa-
710 pore, Singapore, 2010.
711 [31] Y. Zhong and X. Chen, "An FFT twofold subspace-based optimization
712 method for solving electromagnetic inverse scattering problems," *IEEE
713 Trans. Antennas Propag.*, vol. 59, no. 3, pp. 914–927, Mar. 2011.
714 [32] T. Isernia, V. Pascazio, and R. Pierri, "A nonlinear estimation method in
715 tomographic imaging," *IEEE Trans. Geosci. Remote Sens.*, vol. 35, no. 4,
716 pp. 910–923, Jul. 1997.
717 [33] O. M. Bucci, L. Crocco, T. Isernia, and V. Pascazio, "Inverse scatter-
718 ing problems with multifrequency data: Reconstruction capabilities and
719 solution strategies," *IEEE Trans. Geosci. Remote Sens.*, vol. 38, no. 4,
720 pp. 1749–1756, Jul. 2000.
721 [34] R. Pierri, G. Rubinacci, A. Tamburino, S. Ventre, and F. Villone, "Non-
722 linear inverse resistivity profiling using wavelets," *IEEE Trans. Magn.*,
723 vol. 34, no. 5, pp. 2920–2923, Sep. 1998.
724 [35] P. Van den Berg and R. Kleinman, "A total variation enhanced modified
725 gradient algorithm for profile reconstruction," *Inverse Problems*, vol. 11,
726 no. 3, pp. L5–L10, Jun. 1995.
727 [36] J.-M. Geffrin, P. Sabouroux, and C. Eyraud, "Free space experimental
728 scattering database continuation: Experimental set-up and measurement
729 precision," *Inverse Problems*, vol. 21, no. 6, pp. S117–S130, Dec. 2005.
730 [37] R. F. Bloemenkamp, A. Abubakar, and P. M. van den Berg, "Inversion
731 of experimental multi-frequency data using the contrast source inversion
732 method," *Inverse Problems*, vol. 17, no. 6, pp. 1611–1622, Dec. 2001.

Kuiwen Xu received the B.S. degree from Hangzhou Dianzi University, Hangzhou, China, in 2009. He is currently working toward the Ph.D. degree in the Laboratory of Applied Research on Electromagnetics, Zhejiang University, Hangzhou.

During 2012–2013, he was a Visiting Scholar with the National University of Singapore, Singapore. His recent research interests include microwave circuit, array antennas, and inverse scattering problems.



Yu Zhong was born in Guangdong, China, in 1980. 742 He received the B.S. and M.S. degrees in electronic 743 engineering from Zhejiang University, Hangzhou, 744 China, in 2003 and 2006, respectively, and the Ph.D. 745 degree from the National University of Singapore, 746 Singapore, in 2010. 747

He is currently a Scientist with the Institu- 748 tion of High Performance Computing, A*STAR, 749 Singapore. In 2012 and 2013, he was an Invited 750 Senior Scientific Expert with the Laboratoire des 751 Signaux et Systèmes, Gif-sur-Yvette, France. His 752 research interests include inverse scattering problems and electromagnetic 753 modeling on composite materials. 754



Rencheng Song received the B.S. degree in 755 computational mathematics from Jilin University, 756 Changchun, China, in 2005 and the Ph.D. de- 757 gree from Zhejiang University, Hangzhou, China, 758 in 2010. 759

From July 2010 to January 2013, he was with the 760 Department of Electrical and Computer Engineering, 761 National University of Singapore, Singapore. He is 762 currently a Principal Scientist with Halliburton Far 763 East Pte. Ltd., Singapore. His research interests in- 764 clude electromagnetic inverse problems, particularly 765 well-logging applications. 766



Xudong Chen (M'09) received the B.S. and M.S. 767 degrees in electrical engineering from Zhejiang Uni- 768 versity, Hangzhou, China, in 1999 and 2001, respec- 769 tively, and the Ph.D. degree from the Massachusetts 770 Institute of Technology, Cambridge, MA, USA, 771 in 2005. 772

Since then, he joined the Department of Electrical 773 and Computer Engineering, National University of 774 Singapore, Singapore, where he is currently an As- 775 sociate Professor. In 2010, he was an invited Visiting 776 Associate Professor with the University of Paris- 777 SUD 11. During 2012–2013, he took a sabbatical leave at Stanford University, 778 Stanford, CA, USA, where he worked on microwave impedance tomography. 779 He has published more than 100 journal papers on inverse scattering problems, 780 material parameter retrieval, and optimization algorithms. His research interests 781 mainly include electromagnetic inverse problems. 782

Dr. Chen was the recipient of the Young Scientist Award by the Union Radio- 783 Scientifique Internationale in 2010. 784



Lixin Ran received the B.S., M.S., and Ph.D. de- 785 grees from Zhejiang University, Hangzhou, China, in 786 1991, 1994, and 1997, respectively. 787

In 1997, he became an Assistant Professor; in 788 1999, an Associate Professor; and in 2004, a Full 789 Professor with the Department of Information and 790 Electronics Engineering, Zhejiang University. He is 791 currently the Director of the Laboratory of Applied 792 Research on Electromagnetics (ARE), Zhejiang Uni- 793 versity. In 2005, 2009, and 2012, he was a Visiting 794 Scientist with the Massachusetts Institute of Tech- 795

nology, Cambridge, MA, USA. He has coauthored over 120 research papers 796 published in peer-reviewed journals. He holds over 30 patents. His research 797 interests include new concept antennas; radio-aware sensing and imaging; radio 798 frequency, microwave, and terahertz systems; and artificial active media. 799

AUTHOR QUERIES

AUTHOR PLEASE ANSWER ALL QUERIES

Please be aware that authors are required to pay overlength page charges (\$200 per page) if the paper is longer than 6 pages. If you cannot pay any or all of these charges please let us know.

This pdf contains 2 proofs. The first half is the version that will appear on Xplore. The second half is the version that will appear in print. If you have any figures to print in color, they will be in color in both proofs.

The “Open Access” option for your paper expires when the paper is published on Xplore in an issue with page numbers. Papers in “Early Access” may be changed to Open Access.

AQ1 = Note that Fig. 2 was uncited in the original text. Please check if the suggested text citation for Fig. 2 is appropriate. Otherwise, kindly provide the necessary corrections.

AQ2 = Please provide issue number and month of publication.

END OF ALL QUERIES

IEEE Proof